Title: Citizen seismology helps decipher the 2021 Haiti earthquake

Authors:

E. Calais[1,2,3,4,*], S. Symithe[3,5], T. Monfret[2,3,11], B. Delouis[2,3], A. Lomax[6], F. Courboulex[2,3], J.P. Ampuero[2,3], P.E. Lara[2,7], Q. Bletery[2,3], J. Chèze[2,3], F. Peix[2,3], A. Deschamps[2,3], B. de Lépinay[2,3], B. Raimbault[1], R. Jolivet[1,4], S. Paul[2,3,5], S. St Fleur[3,5], D. Boisson[3,5], Y. Fukushima[8], Z. Duputel[9], L. Xu[10], and L. Meng[10]

Affiliations :

[1] Département de Géosciences, École Normale Supérieure, CNRS UMR 8538, PSL Université; Paris, France.

[2] Université Côte d'Azur, Institut de Recherche pour le Développement, Centre National de la Recherche Scientifique, Observatoire de la Côte d'Azur, Géoazur ; Valbonne, France.

[3] CARIBACT Joint Research Laboratory, Université d'État d'Haïti, Université Côte d'Azur, Institut de Recherche pour le Développement; Port-au-Prince, Haïti.

[4] Institut Universitaire de France; Paris, France.

[5] URGéo, Faculté des Sciences, Université d'État d'Haïti; Port-au-Prince, Haïti.

[6] ALomax Scientific; Mouans Sartoux, France.

[7] Instituto Geofísico del Perú; Lima, Perú.

[8] International Research Institute of Disaster Science, Tohoku University; Sendai, Japan.

[9] Observatoire Volcanologique du Piton de la Fournaise, Université de Paris, Institut de Physique du Globe de Paris, CNRS; Paris, France.

[10] Department of Earth, Planetary and Space Sciences, University of California; Los Angeles, CA, USA.

[11] Barcelona Center for Subsurface Imaging, Institut de Ciències del Mar (ICM), CSIC, Barcelona, Spain.

*Corresponding author. Email: eric.calais@ens.fr.

Abstract:

The August 14, Mw7.2, Nippes earthquake in Haiti occurred within the same fault zone as its devastating, Mw7.0, 2010 predecessor but struck the country when field access was limited by insecurity and conventional seismometers from the national network were inoperative. A network of citizen seismometers installed in 2019 provided near-field data critical to rapidly understand the mechanism of the mainshock and monitor its aftershock sequence. Their real-time data define two aftershock clusters that coincide with two areas of coseismic slip derived from inversions of conventional seismological and geodetic data. Machine learning applied to data from the citizen seismometer closest to the mainshock allows us to forecast aftershocks as accurately as with the network-derived catalog. This shows the utility of citizen science contributing to the understanding of a major earthquake.

One-Sentence Summary:

A major earthquake in Haiti was monitored thanks to low-cost, citizen-hosted seismometers, providing a rapid evaluation of the event.

Main text:

On August 14 2021, a M_w7.2 earthquake struck the Southern Peninsula of Haiti (Fig. 1A), leaving ~2,500 dead, 13,000 injured, at least 140,000 houses destroyed or damaged, and a number of water, sanitation and health facilities severely affected *(1)*. Because it affected an area that is mostly rural, with low population density, its impact was much lower than the smaller, but devastating, January 12, 2010, M_w7.0 Haiti event (*2,3,4*). Most of the damage and casualties are concentrated in the populated cities of Les Cayes and Jérémie (Fig. 1B), but hard-to-reach rural communities also took their toll, in a context aggravated by the tropical storm that followed the event and chronic insecurity complicating field access from the capital city. In spite of these difficulties, and in the absence of an operational national network of conventional seismic stations, nearby seismological data were readily available during and after the earthquake because of a citizen seismology effort using inexpensive and low-maintenance "Raspberry Shake" (RS) seismic stations hosted by volunteers (*5,6,7*) (Fig. 1) (see 8, section 1), with two original goals. The first was to install simple but scientifically useful seismological sensors in the homes of citizens to improve the dissemination of seismological information to the public, increase earthquake awareness, and promote grassroots protection initiatives (8). The second was to complement the national broad-band seismological network, a high-technology system difficult to operate and maintain in a development context with a chronic lack of state resources. This citizen-based seismic network bears similarities with the Quake Catcher and Community Seismic networks deployed in California (*9,10)*, though these use accelerometers only and are deployed in a region already well-covered with conventional seismic stations. The August 14 earthquake and its aftershock sequence are an important test of the applicability of low-cost, citizen-hosted seismometers to provide scientifically-relevant data for the rapid response to a major earthquake.

The 2021 Nippes earthquake occurred within the Caribbean-North American plate boundary (Fig. 1A), where the two plates are converging obliquely at a speed of ~2 cm/yr (*11*). The convergence component of plate motion is accommodated by the underthrusting of north American oceanic lithosphere along the Puerto Rico Trench – North Hispaniola fault, while the left-lateral component is accommodated by the Septentrional and Enriquillo strike-slip fault zones (*12,13,14*). The Enriquillo fault zone is considered the source of at least 3 major historical earthquakes in 1701 (M_I6.6), 1751 (M_I7.4) and 1770 (M_I7.5), and a fourth, smaller one in 1860 with M_I6.3 (*15,16)* (Fig. 1A). It was also the locus of the devastating M_w7.0 earthquake of January 12, 2010. The epicentral region of the 2021 Nippes earthquake experienced two significant events in 1952 (M_w6.1) and 1953 (M_w6.0) *(17)* and recurring clusters of smaller felt events, as in 2015 for instance *(18)*.

The mainshock was detected and characterized within minutes, with a moment magnitude of M_w7.2, consistent across most seismological agencies, 40% more energetic than the 2010 event, and with a source mechanism combining strike-slip and reverse faulting (*19*). It was recorded by five seismometers in Haiti, three RS hosted by citizens, and two conventional stations in Port-au-Prince, about 120 km from the epicenter, one USGS accelerometer in the American embassy and one educational broadband instrument in a high school (*20*). RS station R50D4, located 21 km from the epicenter (Fig. 1B), includes accelerometric sensors which recorded the mainshock without saturation with a maximum peak ground acceleration of 0.33 g on its north-south component (Fig. 2A). The high acceleration values for pseudo periods lower than 0.5 s (Fig. 2C) (see 8, section 2) likely explains the severity of damages observed in the epicentral area in houses that, for the most, were not built to earthquake-resistant standards. Spectral acceleration

with 5% damping slightly exceeds the current Haiti building code (*21,22*) (Fig. 2C), indicating that even constructions built to current standards were exposed to an unexpectedly-high hazard.

We determined a source mechanism for the mainshock using a linear finite-source model and the waveform inversion of data from conventional seismic stations at regional distance plus the near-source 3-component accelerometric record from RS station R50D4 (Fig. 2B) (see 8, section 3). The mechanism, consistent with global seismological agencies *(19)*, combines 45% of strike-slip and 55% of reverse moment release, with an east-west trending nodal plane consistent with the local strike of the Enriquillo fault, and dipping 60° to the north (Fig. 1B). The optimal centroid source depth is 6 km, indicating that most of the seismic moment was released at shallow depth. The citizen network detected two events of specific interest in the near vicinity of the mainshock. A possible foreshock on April 6, 2021, Ml4.5, coincides with the mainshock location, with a similar source mechanism (Fig. 1B). A significant aftershock (08/25, M_l4.6) detected by 4 RS stations is located within a few km of the mainshock with a purely reverse mechanism (Fig. 1B). The 3-component accelerometric recordings of the RS instruments were too noisy to be exploited at low frequency for these two smaller events, but their vertical velocimetric component contributed to the waveform inversion.

As of Sep 9, 2021, the citizen-based seismic network, together with regional conventional seismic stations located more than 120 km from the epicenter, detected 1031 aftershocks within a magnitude range of M_l1.4 to 5.8, with a completeness magnitude around M_l2.8. For comparison, 37 aftershocks are available for the same period in the global USGS catalog *(23)*, which targets M4.5+ earthquakes only outside of the U.S. We precisely relocated the mainshock and its aftershocks using manual (70% of events) and automatic P and S arrival picks, source-specific station terms and waveform similarity *(24)*, with estimated error in absolute positions of 5-8 km and relative positions between nearby events of as little as 2 km (see 8, section 4). We show the 732 higher-quality aftershock locations in Fig. 1B and 3A. We used only P-wave arrivals for the precise mainshock relocation, since S-wave arrivals for large events are hidden in the P-wave train, and obtained the hypocenter at 18.42°N/73.51°W and 19 km depth.

Aftershocks are mostly located to the north of the Enriquillo fault (Fig. 1B and 3A), with densest activity extending ~50 km E-W in two separate clusters: an eastern NW oriented cluster with ~4–20 km depth range, ~10x25 km^2 area and overall dip to the NNE, containing the mainshock hypocenter at its base, and a western NE oriented cluster with ~5x15 km^2 area and most events shallower than ~10 km depth. The western cluster merges westwards into a sparse, E-W trend of events extending up to ~30 km along the Enriquillo fault zone, giving a total E-W extent of the main aftershock activity of as much as 80 km. Relocation without the citizen-based seismic network gives almost no depth constraint and produces a featureless cloud of epicenters of about 80 km extent and shifted ~20 km NE of the centroid of the precisely located seismicity clusters.

The real-time detection of a large number of aftershocks permitted by the citizen-based seismic network allowed us to forecast their decay rates in a timely manner, an information useful to the local population and emergency responders. The Reasenberg-Jones method *(25)* applied to the first twelve hours of the aftershock catalogue shows a good match between the observed and forecast aftershock rates, which agree within 95% confidence over a 25-day interval (see 8, section 5). In addition, we used a Machine Learning (ML) approach to build an independent aftershock catalog using a single RS station (R50D4) (see 8, section 5). These two independent catalogs are in good agreement, as well as the aftershock forecasts derived from each of them (Fig. 2D). This indicates that a single, well-located RS can provide the same forecast as the full network, maybe even a better one at very early times (Figure S6). This highlights the potential of

low-cost instrumentation combined with ML for earthquake risk reduction in seismically active regions with limited resources.

We computed a kinematic finite fault slip model using regional broad-band and strong-motion data, including near-field data from the R50D4 accelerometer (Fig. 3B) (see 8, section 6). The rupture propagated unilaterally from the hypocenter westward over a distance of 50 to 60 km, at an average velocity of 2.8 km/s, with two areas of larger slip that correspond to the two aftershock clusters described above. The first area of large slip, to the east, is about 30 km-long, with largely dominant reverse motion between 0 and 12 km depth. The second area of large slip, to the west, is limited to shallow depth (0 to 4 km) with pure left-lateral motion. The source time function indicates a rupture duration of about 20 s, followed by a small, separated, and less-well constrained burst near the western termination of the rupture. Teleseismic back-projection source imaging (see 8, section 7) yields first-order rupture characteristics consistent with the kinematic source inversion results, with a 50-60 km-long rupture propagating unilaterally westward at an average speed of about 3 km/s (Fig. 3D). This consistency relies on calibrating seismic ray propagation paths using aftershock data to account for local structure heterogeneity. The accuracy of the aftershock locations, thanks to citizen-based seismic stations, was essential to ensure the quality of the calibration.

We confirmed the seismic source mechanism using independent geodetic data available with a few weeks delay (see 8, section 8). Radar interferograms from the Sentinel 1 A and B and ALOS-2 satellites show (1) significant vertical motion in the epicentral area, consistent with thrusting on a north-dipping structure (Fig. 1B), (2) a rupture that reached the surface along the previously mapped Ravine du Sud fault (*26*) (Fig. 1B) but remained blind otherwise. A non-linear least-squares search for the rupture geometry considering two rectangular fault planes (see 8, section 9) finds best-fit planes that coincide with the two aftershock clusters described above (Fig. 1B and 3A). A north-dipping (~60°N) plane in the eastern part of the epicentral region shows a combination of reverse and strike-slip motion, with a surface trace that coincides with the Enriquillo fault. A steeper (~71°N) north-dipping plane to the west shows mostly strike-slip motion, with a surface trace that coincides with the Ravine du Sud fault.

Given the coincidence between the non-linear inversion rupture and the surface expression of the Enriquillo and Ravine du Sud faults, we used their mapped traces to build north-dipping rupture geometries at depth and infer the distribution of coseismic slip along them (Fig. 3C) (see 8, section 10). The resulting InSAR slip distribution is consistent with the rupture of two main patches, coinciding with the relocated aftershocks (Fig. 3A) and with the finite fault seismic model (Fig. 3B). This consistency highlights the value of RS data to rapidly assess the main characteristics of this earthquake sequence.

In the slip models, the main patch to the east coincides with the mainshock epicenter location, with slip reaching 1.9 m, dominated by reverse motion. A second patch to the east coincides with the Ravine du Sud fault, with up to 2.3 m of purely strike-slip motion. The focal mechanisms corresponding to these two slip patches, highlighted by the aftershock distribution, are within uncertainties of those estimated independently from long period modelling considering two point-sources (Fig. 3C) (see 8, section 11).

We used this coseismic slip model, together with that of the 2010 earthquake (*27,28*), to compute the Coulomb failure stress (CFS, Fig. 4) imparted on faults of similar orientation and kinematics as the main, strike-slip Enriquillo fault (see 8, section 12). The initiation area of the 2021 rupture falls within an area of increased CFS caused by the 2010 event, an indication that the two

earthquakes may be part of a sequence where the 2010 event triggered the 2021 earthquake, as observed on other major strike-slip fault systems. The aftershock distribution of the two earthquakes shows that their ruptures are not contiguous. The ~60 km—long fault segment between them, as well as other segments to the west and east, have not ruptured in a significant earthquake since at least the series of four events in the 18th century (*16*) and show increased CFS (Fig. 4). The 2010 and 2021 events have therefore increased earthquake hazard in southern Haiti, an information critical to long-term planning for the region.

The 2021 Nippes earthquake bears similarities with the 2010 event (*2,3,27,28*). They both exhibit aftershocks and coseismic slip north of the Enriquillo fault, initiate with a significant component of reverse faulting motion on an eastern segment, and propagate westward with later, mostly strike-slip motion. Their significant dip-slip moment release is intriguing given the mainly strike-slip motion recorded geologically on the Enriquillo fault, an information hard-wired into Haiti's seismic hazard map (*21*). It is consistent, however, with interseismic geodetic measurements (*11,29,30*) (Fig. 1B) and onshore/offshore geophysical data (*31,32,33*) that show a far-field kinematics combining strike-slip and convergence, with NNE-SSW–directed compression. A reappraisal of the seismic hazard map of Haiti is therefore in order to account for this significant N-S shortening component and provide updated information for building code purposes.

The rapid assessment of the source mechanism, near-field ground shaking, and aftershock distribution of the 2021 Nippes earthquake was made possible by inexpensive seismometers hosted by citizens, together with information from classic seismological and geodetic data and models. The inclusion of the RS data in waveform inversions shows that they provide data of sufficient quality for adding valuable near-source information into the slip model, as confirmed by the InSAR slip inversion. This is an important example of a direct impact of citizen seismology to understand a large and damaging earthquake in the absence of conventional seismic stations in the near-field of the event, highlighting the added-value of citizen seismology for rapid earthquake response. The high benefit to cost ratio of citizen seismology makes it particularly relevant to regions of similar socio-economic level as Haiti, where the implementation of conventional seismic networks operated by official institutions may be difficult *(34)*.

References and Notes:

1. UN Office for the Coordination of Humanitarian Affairs, "Haïti: Tremblement de terre Rapport de Situation No. 2 Au 26 Août 2021" (OCHA, 2021); https://reliefweb.int/report/haiti/ha-ti-tremblement-de-terre-rapport-de-situation-no-2-au-26-ao-t-2021
2. E. Calais, A. Freed, G. Mattioli, F. Amelung, S. Jónsson, P. Jansma, S.-H. Hong, T. Dixon, C. Prépetit, R. Momplaisir, Transpressional rupture of an unmapped fault during the 2010 Haiti earthquake. *Nat. Geosci.* **3**, 794–799 (2010). doi:10.1038/ngeo992
3. G. P. Hayes, R. W. Briggs, A. Sladen, E. J. Fielding, C. Prentice, K. Hudnut, P. Mann, F. W. Taylor, A. J. Crone, R. Gold, T. Ito, M. Simons, Complex rupture during the 12 January 2010 Haiti earthquake. *Nat. Geosci.* **3**, 800–805 (2010). doi:10.1038/ngeo977
4. M. Hashimoto, Y. Fukushima, Y. Fukahata, Fan-delta uplift and mountain subsidence during the Haiti 2010 earthquake. *Nat. Geosci.* **4**, 255–259 (2011). doi:10.1038/ngeo1115

5. E. Calais, D. Boisson, S. Symithe, C. Prépetit, B. Pierre, S. Ulyse, L. Hurbon, A. Gilles, J.-M. Théodat, T. Monfret, A. Deschamps, F. Courboulex, J. Chèze, F. Peix, E. Bertrand, J.-P. Ampuero, B. Mercier de Lépinay, J. Balestra, J.-L. Berenguer, R. Bossu, L. Fallou, V. Clouard, A socio-seismology experiment in Haiti. *Front. Earth Sci. (Lausanne)* **8**, 542654 (2020). doi:10.3389/feart.2020.542654

6. R. E. Anthony, A. T. Ringler, D. C. Wilson, E. Wolin, Do low-cost seismographs perform well enough for your network? An overview of laboratory tests and field observations of the OSOP Raspberry Shake 4D. *Seismol. Res. Lett.* **90**, 219–228 (2018). doi:10.1785/0220180251

7. Ayiti-Séismes Project, "Prognosis on 08/23/2021 of the aftershocks of the Nippes earthquake, Haiti (08/14/2021, magnitude 7.2)" (Ayiti-Séismes Project, 2021); https://ayiti.unice.fr/ayiti-seismes/

8. L. Fallou, E. Calais, A. Corbet, L. Hurbon, and J.M. Théodat, Citizen-seismology in Haiti, understanding citizens' interest and beliefs to enhance community resilience and contribute to risk reduction, paper presented at the Citizen Science SDG Conference: Knowledge for Change: A Decade of Citizen Science (2020-2030) in Support of the Sustainable Development Goals, Berlin, 14–15 October 2020.

9. E. S. Cochran, J. F. Lawrence, C. M. Christensen, R. S. Jakka, The Quake-catcher network: Citizen science expanding seismic Horizons. *Seismol. Res. Lett.* **80**, 26–30 (2009). doi:10.1785/gssrl.80.1.26

10. R. W. Clayton, T. Heaton, M. Chandy, A. Krause, M. Kohler, J. Bunn, R. Guy, M. Olson, M. Faulkner, M. Cheng, L. Strand, R. Chandy, D. Obenshain, A. Liu, M. Aivazis, Community seismic network. *Ann. Geophys.* **54**, 6 (2011). doi:10.4401/ag-5269

11. S. Symithe, E. Calais, J. B. de Chabalier, R. Robertson, M. Higgins, Current block motions and strain accumulation on active faults in the Caribbean. *J. Geophys. Res. Solid Earth* **120**, 120 (2015). doi:10.1002/2014JB011779

12. P. Mann, F. W. Taylor, R. L. Edwards, T. L. Ku, Actively evolving microplate formation by oblique collision and sideways motion along strike-slip faults: An example from the northeastern Caribbean plate margin. *Tectonophysics* **246**, 1–69 (1995). doi:10.1016/0040-1951(94)00268-E

13. E. Calais, Y. Mazabraud, B. Mercier de Lépinay, P. Mann, G. Mattioli, P. Jansma, Strain partitioning and fault slip rates in the northeastern Caribbean from GPS measurements. *Geophys. Res. Lett.* **29**, 1856 (2002). doi:10.1029/2002GL015397

14. P. Mann, E. Calais, J.-C. Ruegg, C. DeMets, P. E. Jansma, G. S. Mattioli, Oblique collision in the northeastern Caribbean from GPS measurements and geological observations. *Tectonics* **21**, 7–26 (2002). doi:10.1029/2001TC001304

15. J. Scherer, Great earthquakes in the island of Haiti. *Bull. Seismol. Soc. Am.* **2**, 161–180 (1912). doi:10.1785/BSSA0020030161

16. W. H. Bakun, C. H. Flores, U. S. ten Brink, Significant earthquakes on the Enriquillo fault system, Hispaniola, 1500-2010: Implications for seismic hazard. *Bull. Seismol. Soc. Am.* **102**, 18–30 (2012). doi:10.1785/0120110077

17. I. Bondár, E. R. Engdahl, A. Villaseñor, J. Harris, D. Storchak, ISC-GEM: Global instrumental earthquake catalogue (1900–2009), II. Location and seismicity patterns. *Phys. Earth Planet. Inter.* **239**, 2–13 (2015). doi:10.1016/j.pepi.2014.06.002

18. C. Prépetit, Anse-à-Veau, la ville sismique oubliée, published by the Bureau of Mines and Energy, Haiti, January 2016, http://www.bme.gouv.ht/uts/Anse-à-Veau.pdf.

19. European-Mediterranean Seismological Centre, "M 7.2 - HAITI REGION - 2021-08-14 12:29:09 UTC" (EMSC, 2021); https://www.emsc-csem.org/Earthquake/earthquake.php?id=1023410#map

20. F. Courboulex, J. L. Berenguer, A. Tocheport, M. P. Bouin, E. Calais, Y. Esnault, C. Larroque, G. Nolet, J. Virieux, Sismos à l'ecole: A worldwide network of real-time seismometers in schools. *Seismol. Res. Lett.* **83**, 870–873 (2012). doi:10.1785/0220110139

21. A. Frankel, S. Harmsen, C. Mueller, E. Calais, J. Haase, Seismic hazard maps for Haiti. *Earthq. Spectra* **27** (1_suppl1), S23–S41 (2011). doi:10.1193/1.3631016

22. Ministère des Travaux Publics, Transports et Communications, "Code National du Bâtiment d'Haït (CNBH) 2012" (MTPTC, 2013); https://www.mtptc.gouv.ht/media/upload/doc/publications/CNBH_fusion.pdf

23. US Geological Survey, "Search earthquake catalog" (USGS, 2022); https://earthquake.usgs.gov/earthquakes/search/

24. A. Lomax, A. Savvaidis, High-precision, absolute earthquake location using source-specific station terms and inter-event waveform similarity. *J. Geophys. Res. Solid Earth* **127**, e2021JB023190 (2022). doi:10.1029/2021JB023190

25. P. A. Reasenberg, L. M. Jones, Earthquake hazard after a mainshock in California. *Science* **243**, 1173–1176 (1989). doi:10.1126/science.243.4895.1173

26. N. Saint Fleur, N. Feuillet, Y. Klinger, Active tectonics along the Cul-de-Sac – Enriquillo plain and seismic hazard for Port-au-Prince, Haiti. *Tectonophysics* **771**, 228235 (2019). doi:10.1016/j.tecto.2019.228235

27. S. J. Symithe, E. Calais, J. S. Haase, A. M. Freed, R. Douilly, Coseismic slip distribution of the 2010 M 7.0 Haiti earthquake and resulting stress changes on regional faults. *Bull. Seismol. Soc. Am.* **103**, 2326–2343 (2013). doi:10.1785/0120120306

28. R. Douilly, J. S. Haase, W. L. Ellsworth, M.-P. Bouin, E. Calais, S. J. Symithe, J. G. Armbruster, B. M. de Lepinay, A. Deschamps, S.-L. Mildor, M. E. Meremonte, S. E. Hough, Crustal structure and fault geometry of the 2010 Haiti earthquake from temporary seismometer deployments. *Bull. Seismol. Soc. Am.* **103**, 2305–2325 (2013). doi:10.1785/0120120303

29. B. Benford, C. DeMets, E. Calais, GPS estimates of microplate motions, northern Caribbean: Evidence for a Hispaniola microplate and implications for earthquake hazard. *Geophys. J. Int.* **191**, 481–490 (2012). doi:10.1111/j.1365-246X.2012.05662.x

30. S. Symithe, E. Calais, Present-day shortening in Southern Haiti from GPS measurements and implications for seismic hazard. *Tectonophysics* **679**, 117–124 (2016). doi:10.1016/j.tecto.2016.04.034

31. J. Rodriguez, J. Havskov, M. B. Sørensen, L. F. Santos, Seismotectonics of south-west Dominican Republic using recent data. *J. Seismol.* **22**, 883–896 (2018). doi:10.1007/s10950-018-9738-9

32. D. Possee, D. Keir, N. Harmon, C. Rychert, F. Rolandone, S. Leroy, J. Corbeau, G. Stuart, E. Calais, F. Illsley-Kemp, D. Boisson, R. Momplaisir, C. Prépetit, The tectonics and active faulting of Haiti from seismicity and tomography. *Tectonics* **38**, 1138–1155 (2019). doi:10.1029/2018TC005364

33. J. Corbeau, F. Rolandone, S. Leroy, B. Meyer, B. Mercier de Lépinay, N. Ellouz-Zimmermann, R. Momplaisir, How transpressive is the northern Caribbean plate boundary? *Tectonics* **35**, 1032–1046 (2016). doi:10.1002/2015TC003996

34. S. Subedi, G. Hetényi, P. Denton, A. Sauron, Seismology at school in Nepal: A program for educational and citizen seismology through a low-cost seismic network. *Front. Earth Sci. (Lausanne)* **8**, 73 (2020). doi:10.3389/feart.2020.00073

35. Helmholtz-Centre Potsdam - GFZ German Research Centre for Geosciences and gempa GmbH (2008). The SeisComP seismological software package. GFZ Data Services. https://doi.org/10.5880/GFZ.2.4.2020.003.

36. B. Delouis, FMNEAR: Determination of focal mechanism and first estimate of rupture directivity using near-source records and a linear distribution of point sources. *Bull. Seismol. Soc. Am.* **104**, 1479–1500 (2014). doi:10.1785/0120130151

37. M. Bouchon, A simple method to calculate Green's functions for elastic layered media. *Bull. Seismol. Soc. Am.* **71**, 959–971 (1981). doi:10.1785/BSSA0710040959

38. A. Lomax, J. Virieux, P. Volant, C. Berge-Thierry, "Probabilistic earthquake location in 3D and layered models," in *Advances in Seismic Event Location*, C. H. Thurber, N. Rabinowitz, Eds. (Springer, 2000); vol. 18, pp. 101–134; https://doi.org/10.1007/978-94-015-9536-0_5

39. A. Lomax, A. Michelini, A. Curtis, "Earthquake location, direct, global-search methods," in *Encyclopedia of Complexity and Systems Science*, R. A. Meyers, Ed. (Springer, 2014); pp. 1–33; https://doi.org/10.1007/978-3-642-27737-5_150-2.

40. Y. Font, H. Kao, S. Lallemand, C.-S. Liu, L.-Y. Chiao, Hypocentre determination offshore of eastern Taiwan using the maximum intersection method. *Geophys. J. Int.* **158**, 655–675 (2004). doi:10.1111/j.1365-246X.2004.02317.x

41. A. Lomax, A reanalysis of the hypocentral location and related observations for the great 1906 California earthquake. *Bull. Seismol. Soc. Am.* **95**, 861–877 (2005). doi:10.1785/0120040141

42. A. Lomax, Location of the focus and tectonics of the focal region of the California earthquake of 18 April 1906. *Bull. Seismol. Soc. Am.* **98**, 846–860 (2008). doi:10.1785/0120060405

43. H. Zhou, Rapid three-dimensional hypocentral determination using a master station method. *J. Geophys. Res.* **99** (B8), 15439 (1994). doi:10.1029/94JB00934

44. P. Podvin, I. Lecomte, Finite difference computation of traveltimes in very contrasted velocity models: A massively parallel approach and its associated tools. *Geophys. J. Int.* **105**, 271–284 (1991). doi:10.1111/j.1365-246X.1991.tb03461.x

45. A. Lomax, A. Savvaidis, "High-precision, absolute earthquake location using source-specific station terms and inter-event waveform similarity" (ESSOAr, 2021); https://www.essoar.org/doi/10.1002/essoar.10507108.1.

46. G. L. Pavlis, N. B. Hokanson, Separated earthquake location. *J. Geophys. Res.* **90** (B14), 12777–12789 (1985). doi:10.1029/JB090iB14p12777

47. K. B. Richards-Dinger, P. M. Shearer, Earthquake locations in southern California obtained using source-specific station terms. *J. Geophys. Res.* **105** (B5), 10939–10960 (2000). doi:10.1029/2000JB900014

48. G. Lin, P. Shearer, Tests of relative earthquake location techniques using synthetic data. *J. Geophys. Res.* **110** (B4), (2005). doi:10.1029/2004JB003380

49. N. Nooshiri, J. Saul, S. Heimann, F. Tilmann, T. Dahm, Revision of earthquake hypocentre locations in global bulletin data sets using source-specific station terms. *Geophys. J. Int.* **208**, 589–602 (2017). doi:10.1093/gji/ggw405

50. W. L. Ellsworth, Bear Valley, California, earthquake sequence of February-March 1972. *Bull. Seismol. Soc. Am.* **65**, 483–506 (1975). doi:10.1785/BSSA0650020483

51. C. Frohlich, An efficient method for joint hypocenter determination for large groups of earthquakes. *Comput. Geosci.* **5**, 387–389 (1979). doi:10.1016/0098-3004(79)90034-7

52. W. Tucker, E. Herrin, H. W. Freedman, Some statistical aspects of the estimation of seismic travel times. *Bull. Seismol. Soc. Am.* **58**, 1243–1260 (1968). doi:10.1785/BSSA0580041243

53. R. J. Geller, C. S. Mueller, Four similar earthquakes in central California. *Geophys. Res. Lett.* **7**, 821–824 (1980). doi:10.1029/GL007i010p00821

54. G. Poupinet, F. Glangeaud, P. Cote, "P-Time delay measurement of a doublet of microearthquakes," in *ICASSP '82. IEEE International Conference on Acoustics, Speech, and Signal Processing* (IEEE, 1982), vol. 7, pp. 1516–1519; https://doi.org/10.1109/ICASSP.1982.1171796

55. B. S. Thorbjarnardottir, J. C. Pechmann, Constraints on relative earthquake locations from cross-correlation of waveforms. *Bull. Seismol. Soc. Am.* **77**, 1626–1634 (1987).

56. M. Cattaneo, P. Augliera, D. Spallarossa, C. Eva, Reconstruction of seismogenetic structures by multiplet analysis: An example of Western Liguria, Italy. *Bull. Seismol. Soc. Am.* **87**, 971–986 (1997).

57. G. Ferretti, An improved method for the recognition of seismic families: Application to the Garfagnana-Lunigiana Area, Italy. *Bull. Seismol. Soc. Am.* **95**, 1903–1915 (2005). doi:10.1785/0120040078

58. M. Ishida, H. Kanamori, The foreshock activity of the 1971 San Fernando earthquake, California. *Bull. Seismol. Soc. Am.* **68**, 1265–1279 (1978). doi:10.1785/BSSA0680051265

59. R. Nadeau, M. Antolik, P. A. Johnson, W. Foxall, T. V. McEvilly, Seismological studies at Parkfield III: Microearthquake clusters in the study of fault-zone dynamics. *Int. J. Rock Mech. Min. Sci. Geomech. Abstr.* **31**, 271 (1994). doi:10.1016/0148-9062(94)90077-9

60. B. P. Goertz-Allmann, S. J. Gibbons, V. Oye, R. Bauer, R. Will, Characterization of induced seismicity patterns derived from internal structure in event clusters. *J. Geophys. Res. Solid Earth* **122**, 3875–3894 (2017). doi:10.1002/2016JB013731

61. R. H. Jones, R. C. Stewart, A method for determining significant structures in a cloud of earthquakes. *J. Geophys. Res.* **102** (B4), 8245–8254 (1997). doi:10.1029/96JB03739

62. Y. Kamer, G. Ouillon, D. Sornette, J. Wössner, Condensation of earthquake location distributions: Optimal spatial information encoding and application to multifractal analysis of south Californian seismicity. *Phys. Rev. E Stat. Nonlin. Soft Matter Phys.* **92**, 022808 (2015). doi:10.1103/PhysRevE.92.022808 Medline

63. J.-L. Got, J. Fréchet, F. W. Klein, Deep fault plane geometry inferred from multiplet relative relocation beneath the south flank of Kilauea. *J. Geophys. Res.* **99** (B8), 15375 (1994). doi:10.1029/94JB00577

64. A. Ito, High resolution relative hypocenters of similar earthquakes by cross-spectral analysis method. *J. Phys. Earth* **33**, 279–294 (1985). doi:10.4294/jpe1952.33.279

65. R. S. Matoza, P. M. Shearer, G. Lin, C. J. Wolfe, P. G. Okubo, Systematic relocation of seismicity on Hawaii Island from 1992 to 2009 using waveform cross correlation and cluster analysis. *J. Geophys. Res. Solid Earth* **118**, 2275–2288 (2013). doi:10.1002/jgrb.50189

66. Y. Nakamura, "A1 moonquakes: source distribution and mechanism," in *Proceedings of the Lunar and Planetary Science Conference* (Pergamon Press, 1978); pp. 3589–3607; https://ci.nii.ac.jp/naid/10006236523/en/.

67. G. Poupinet, W. L. Ellsworth, J. Frechet, Monitoring velocity variations in the crust using earthquake doublets: An application to the Calaveras Fault, California. *J. Geophys. Res.* **89** (B7), 5719–5731 (1984). doi:10.1029/JB089iB07p05719

68. F. Waldhauser, W. L. Ellsworth, A double-difference earthquake location algorithm: Method and application to the Northern Hayward Fault, California. *Bull. Seismol. Soc. Am.* **90**, 1353–1368 (2000). doi:10.1785/0120000006

69. R. Douilly, W. L. Ellsworth, E. Kissling, A. M. Freed, A. Deschamps, B. Mercier de Lépinay, 3-D velocity structure in southern Haiti from local earthquake tomography. *J. Geophys. Res. Solid Earth* **121**, 8813–8832 (2016). doi:10.1002/2016JB013123

70. B. L. N. Kennett, E. R. Engdahl, Traveltimes for global earthquake location and phase identification. *Geophys. J. Int.* **105**, 429–465 (1991). doi:10.1111/j.1365-246X.1991.tb06724.x

71. P. A. Reasenberg, L. M. Jones, Earthquake aftershocks: Update. *Science* **265**, 1251–1252 (1994). doi:10.1126/science.265.5176.1251 Medline

72. T. Utsu, Y. Ogata, R. S, Matsu'ura, The centenary of the Omori formula for a decay law of aftershock activity. *J. Phys. Earth* **43**, 1–33 (1995). doi:10.4294/jpe1952.43.1

73. S. M. Mousavi, Y. Sheng, W. Zhu, G. C. Beroza, STanford EArthquake Dataset (STEAD): A global data set of seismic signals for AI. *IEEE Access* **7**, 179464–179476 (2019). doi:10.1109/ACCESS.2019.2947848

74. T. Chen, T. He, M. Benesty, V. Khotilovich, Y. Tang, H. Cho, "Xgboost: extreme gradient boosting" (R package version 0.4-2, 2015); https://cran.r-project.org/web/packages/xgboost/vignettes/xgboost.pdf .

75. B. Delouis, D. Giardini, P. Lundgren, J. Salichon, Joint inversion of InSAR, GPS, teleseismic and strong motion data for the spatial and temporal distribution of earthquake slip:

Application to the 1999 Izmit Mainshock. *Bull. Seismol. Soc. Am.* **92**, 278–299 (2002). doi:10.1785/0120000806

76. L. Meng, A. Inbal, J. P. Ampuero, A window into the complexity of the dynamic rupture of the 2011 Mw 9 Tohoku-Oki earthquake. *Geophys. Res. Lett.* **38**, L00G07 (2011). doi:10.1029/2011GL048118

77. L. Meng, J. P. Ampuero, Y. Luo, W. Wu, S. Ni, Mitigating artifacts in back-projection source imaging with implications for frequency-dependent properties of the Tohoku-Oki earthquake. *Earth Planets Space* **64**, 1101–1109 (2012). doi:10.5047/eps.2012.05.010

78. L. Meng, A. Zhang, Y. Yagi, Improving back projection imaging with a novel physics-based aftershock calibration approach: A case study of the 2015 Gorkha earthquake. *Geophys. Res. Lett.* **43**, 628–636 (2016). doi:10.1002/2015GL067034

79. P. A. Rosen, E. Gurrola, G. F. Sacco, H. Zebker, "The InSAR scientific computing environment," in *EUSAR 2012; 9th European Conference on Synthetic Aperture Radar* (European Conference on Synthetic Aperture Radar, 2012); pp. 730–733.

80. T. G. Farr, M. Kobrick, Shuttle radar topography mission produces a wealth of data. *Eos* **81**, 583–585 (2000). doi:10.1029/EO081i048p00583

81. H. Fattahi, P. Agram, M. Simons, A network-based enhanced spectral diversity approach for TOPS time-series analysis. *IEEE Trans. Geosci. Remote Sens.* **55**, 777–786 (2016). doi:10.1109/TGRS.2016.2614925

82. R. M. Goldstein, C. L. Werner, Radar interferogram filtering for geophysical applications. *Geophys. Res. Lett.* **25**, 4035–4038 (1998). doi:10.1029/1998GL900033

83. C. W. Chen, H. A. Zebker, Network approaches to two-dimensional phase unwrapping: Intractability and two new algorithms. *J. Opt. Soc. Am. A Opt. Image Sci. Vis.* **17**, 401–414 (2000). doi:10.1364/JOSAA.17.000401 Medline

84. T. Ozawa, E. Fujita, H. Ueda, Crustal deformation associated with the 2016 Kumamoto Earthquake and its effect on the magma system of Aso volcano. *Earth Planets Space* **68**, 186 (2016). doi:10.1186/s40623-016-0563-5

85. A. Jarvis, H. I. Reuter, A. Nelson, E. Guevara, *Hole-Filled Seamless SRTM Data V4* (International Centre for Tropical Agriculture, 2008).

86. F. G. Lemoine, D. Smith, R. Smith, L. Kunz, E. Pavlis, N. Pavlis, S. Klosko, M. Chinn, M. Torrence, R. Williamson, C. Cox, K. Rachlin, Y. Wang, S. Kenyon, R. Salman, R. Trimmer, R. Rapp, S. Nerem, "The development of the NASA GSFC and NIMA Joint Geopotential Model," in *Gravity, Geoid, and Marine Geodesy: International Symposium No. 117, Tokyo, Japan, September 30 – October 5, 1996*, J. Segawa, H. Fujimoto, S. Okubo, Eds. (Springer, 1997), vol 117, pp, 461–469.

87. I. Baran, M. P. Stewart, B. M. Kampes, Z. Perski, P. A. Lilly, Modification to the Goldstein radar interferogram filter. *IEEE Trans. Geosci. Remote Sens.* **41**, 2114–2118 (2003). doi:10.1109/TGRS.2003.817212

88. J. R. Elliott, R. Jolivet, P. J. Gonzalez, J. P. Avouac, J. Hollingsworth, M. P. Searle, V. L. Stevens, Himalayan megathrust geometry and relation to topography revealed by the Gorkha earthquake. *Nat. Geosci.* **9**, 174–180 (2016). doi:10.1038/ngeo2623

89. R. Jolivet, Z. Duputel, B. Riel, M. Simons, L. Rivera, S. E. Minson, H. Zhang, M. A. G. Aivazis, F. Ayoub, S. Leprince, S. Samsonov, M. Motagh, E. J. Fielding, The 2013 Mw~7.7 Balochistan earthquake: Seismic potential of an accretionary wedge. *Bull. Seismol. Soc. Am.* **104**, 1020–1030 (2014). doi:10.1785/0120130313

90. Y. Okada, Internal deformation due to shear and tensile faults in a half-space. *Bull. Seismol. Soc. Am.* **82**, 1018–1040 (1992). doi:10.1785/BSSA0820021018

91. P.-O. Persson, G. Strang, A simple mesh generator in MATLAB. *SIAM Rev.* **46**, 329–345 (2004). doi:10.1137/S0036144503429121

92. L. Zhu, L. Rivera, A note on the dynamic and static displacements from a point source in multilayered media. *Geophys. J. Int.* **148**, 619–627 (2002). doi:10.1046/j.1365-246X.2002.01610.x

93. P. Virtanen, R. Gommers, T. E. Oliphant, M. Haberland, T. Reddy, D. Cournapeau, E. Burovski, P. Peterson, W. Weckesser, J. Bright, S. J. van der Walt, M. Brett, J. Wilson, K. J. Millman, N. Mayorov, A. R. J. Nelson, E. Jones, R. Kern, E. Larson, C. J. Carey, İ. Polat, Y. Feng, E. W. Moore, J. VanderPlas, D. Laxalde, J. Perktold, R. Cimrman, I. Henriksen, E. A. Quintero, C. R. Harris, A. M. Archibald, A. H. Ribeiro, F. Pedregosa, P. van Mulbregt, A. Vijaykumar, A. P. Bardelli, A. Rothberg, A. Hilboll, A. Kloeckner, A. Scopatz, A. Lee, A. Rokem, C. N. Woods, C. Fulton, C. Masson, C. Häggström, C. Fitzgerald, D. A. Nicholson, D. R. Hagen, D. V. Pasechnik, E. Olivetti, E. Martin, E. Wieser, F. Silva, F. Lenders, F. Wilhelm, G. Young, G. A. Price, G.-L. Ingold, G. E. Allen, G. R. Lee, H. Audren, I. Probst, J. P. Dietrich, J. Silterra, J. T. Webber, J. Slavič, J. Nothman, J. Buchner, J. Kulick, J. L. Schönberger, J. V. de Miranda Cardoso, J. Reimer, J. Harrington, J. L. C. Rodríguez, J. Nunez-Iglesias, J. Kuczynski, K. Tritz, M. Thoma, M. Newville, M. Kümmerer, M. Bolingbroke, M. Tartre, M. Pak, N. J. Smith, N. Nowaczyk, N. Shebanov, O. Pavlyk, P. A. Brodtkorb, P. Lee, R. T. McGibbon, R. Feldbauer, S. Lewis, S. Tygier, S. Sievert, S. Vigna, S. Peterson, S. More, T. Pudlik, T. Oshima, T. J. Pingel, T. P. Robitaille, T. Spura, T. R. Jones, T. Cera, T. Leslie, T. Zito, T. Krauss, U. Upadhyay, Y. O. Halchenko, Y. Vázquez-Baeza, SciPy 1.0: Fundamental algorithms for scientific computing in Python. *Nat. Methods* **17**, 26–272 (2020). doi:10.1038/s41592-019-0686-2

94. M. Radiguet, F. Cotton, M. Vergnolle, M. Campillo, B. Valette, V. Kostoglodov, N. Cotte, Spatial and temporal evolution of a long-term slow slip event: The 2006 Guerrero Slow Slip Event. *Geophys. J. Int.* **184**, 816–828 (2010). doi:10.1111/j.1365-246X.2010.04866.x

95. Z. Duputel, L. Rivera, Long-period analysis of the 2016 Kaikoura earthquake. *Phys. Earth Planet. Inter.* **265**, 62–66 (2017). doi:10.1016/j.pepi.2017.02.004

96. J. Ritsema, A. Deuss, H. J. van Heijst, J. H. Woodhouse, S40RTS: A degree-40 shear-velocity model for the mantle from new Rayleigh wave dispersion, teleseismic traveltime and normal-mode splitting function measurements. *Geophys. J. Int.* **184**, 1223–1236 (2011). doi:10.1111/j.1365-246X.2010.04884.x

97. D. Komatitsch, J. Tromp, Spectral-element simulations of global seismic wave propagation—I. *Geophys. J. Int.* **149**, 390–412 (2002). doi:10.1046/j.1365-246X.2002.01653.x

98. R. A. Harris, R. W. Simpson, Changes in static stress on southern California faults after the 1992 Landers earthquake. *Nature* **360**, 251–254 (1992). doi:10.1038/360251a0

99. G. C. P. King, R. Stein, J. Lin, Static stress changes and the triggering of earthquakes. *Bull. Seismol. Soc. Am.* **84**, 935–953 (1994).

Acknowledgments: This project benefits from the collaboration of citizen seismologists in Haiti and the extra help of seismologists from Géoazur for manual picking of the aftershocks. J. Haase provided comments that improved an early version of the manuscript. ALOS-2 data were provided from JAXA through the Earthquake Working Group coordinated by the Geospatial Information Authority of Japan and JAXA. We acknowledge seismic data from regional networks in the Dominican Republic, Cuba, Jamaica, and Alaska and thank their operating agencies for making them available.

Funding:

Centre National de la Recherche Scientifique (CNRS) and the Institut de Recherche pour le Développement (IRD) through their "Natural Hazard" program (EC, SS, TM, BD, FC, JPA, JC, AD, DB, SP).

FEDER European Community program within the Interreg Caraïbes "PREST" project (EC, SS, DB).

Institut Universitaire de France (EC, RJ).

Université Côte d'Azur and the French Embassy in Haiti (SP).

European Research Council (ERC) under the European Union's Horizon 2020 research and innovation program, Grant Agreement 758210, Geo4D project (RJ).

French National Research Agency (ANR), ANR-21-CE03-0010, "OSMOSE" project (EC).

European Research Council (ERC) under the European Union's Horizon 2020 research and innovation program, Grant Agreement 949221 (QB).

HPC resources of IDRIS under allocations 2020-AD011012142, 2021-AP011012536, and 2021-A0101012314 (QB).

French National Research Agency (ANR), ANR-15-IDEX-01, "UCAJEDI Investments in the Future" (QB).

European Research Council (ERC) under the European Union's Horizon 2020 research and innovation program, Grant Agreement 805256 (ZD).

Author contributions:

Study design and coordination: EC

Citizen-seismology data: SS, SSF, and DB

Main- and after-shock bulletins: SP, FC, TM, AD, VC, JC, FP

Relocated earthquake catalogue: AL

Machine Learning-based aftershock detections: PL, QB

Point source, linear, and kinematic models: BD

Aftershock forecast analysis: JPA

RS50D spectral analysis: FC

Source back-projection: LX, LM

InSAR analysis and resulting fault model: RJ, BR

Multiple point source solution: ZD

ALOS-2 interferograms processing: YF

Writing – original version: all authors

Competing interests: Authors declare that they have no competing interests.

Data and materials availability: All data and code used in this study are openly available. RADAR data can be obtained through ESA (Sentinel) or JAXA (Alos-2). Aftershock data can be obtained from https://ayiti.unice.fr/ayiti-seismes/ (7). The codes used to process or model the data are published and public (8). The catalog of high-precision earthquake relocated with the NLL-SSST-coherence procedure (SM4) is available as supplementary data.

Supplementary Materials:

Materials and Methods

Supplementary Text

Figs. S1 to S26

Captions for Data S1

Data S1

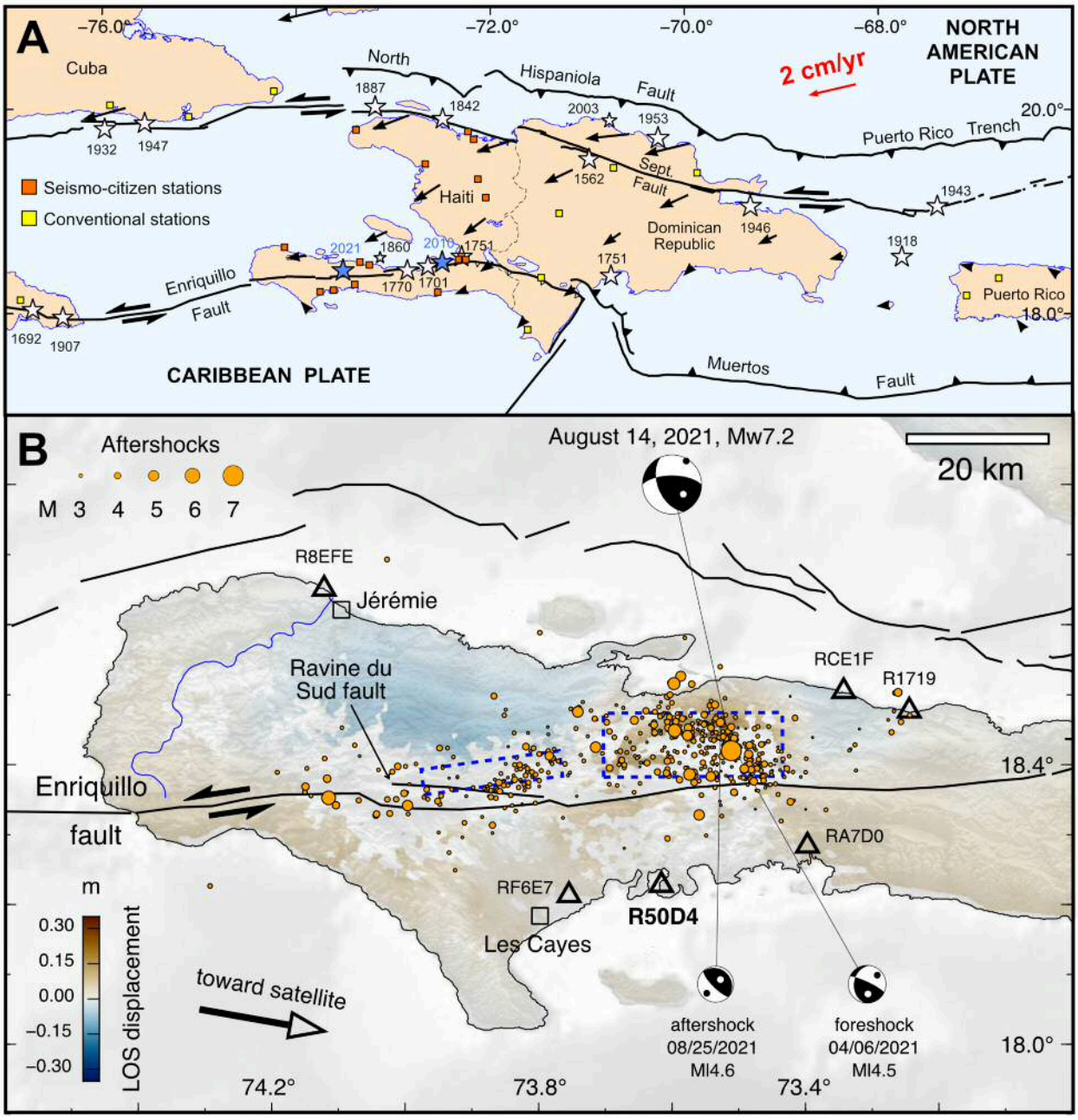

Fig. 1. Seismotectonic context of the 2021 Nippes earthquake. (A) Major active faults of the Caribbean – North America plate boundary zone with historical earthquakes (16) (stars) and Global Positioning System (GPS) velocities (black arrows) with respect to the Caribbean plate (11). (B) Relocated aftershock sequence (14 August to 9 September, 2021) on top of a descending Sentinel interferogram spanning 03 – 08 August 2021. Triangles show citizen-hosted seismometers spanning the epicentral area. Line-of-sight (LOS) ground displacement north of the Enriquillo fault shows motion toward the satellite in the epicentral region (brown) and away from the satellite along the western part of the rupture (blue). Such reversal of the sense of motion along the LOS direction indicates significant vertical motion in the epicentral region and almost pure horizontal, left-lateral motion to the west. Grey areas are not sufficiently coherent to ensure reliable phase unwrapping.

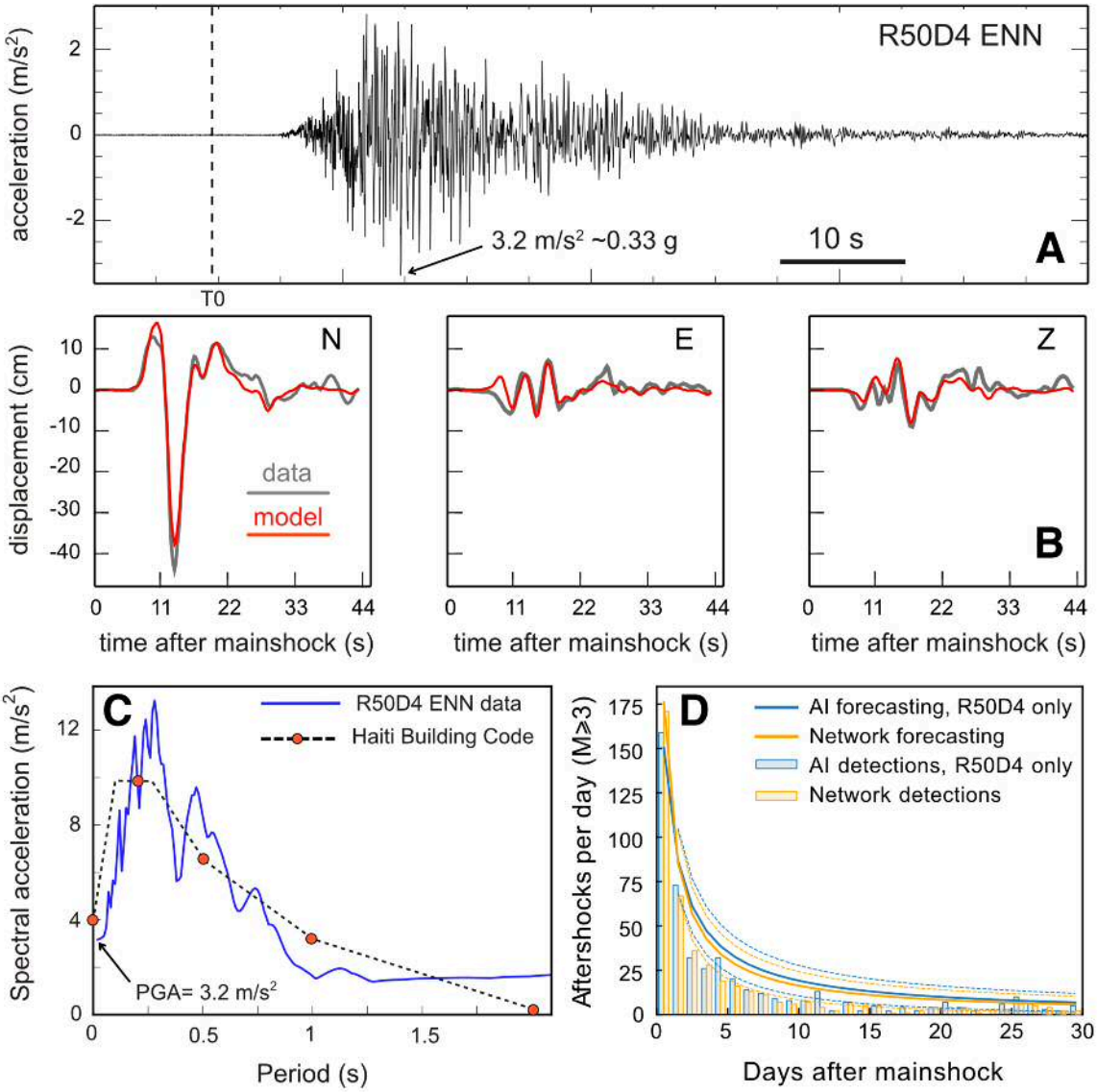

Fig. 2. Data and inferences from citizen station R50D4, 21 km from the 2021 Nippes earthquake rupture. (A) Signal in acceleration of the north component (channel ENN), which recorded a peak ground acceleration (PGA) of 0.33 g. Vertical line labelled T0 indicates the earthquake origin time. (B) Waveform fitting of the 3 components integrated to displacement and bandpass-filtered between 0.06 and 0.5 Hz (N: north, E: east, Z: vertical up). The gray line is the observed signal, the red line is the signal computed with the kinematic finite source model (Fig. 3B). (C) Spectral acceleration with 5% damping (blue line) of the north-south component of ground acceleration at station (Fig. 1B), calculated with a damping of 5%. Red dots indicate the spectral values derived from the Haitian building code for the city of Les Cayes, closest to R50D4 and at the same distance from the rupture. The dashed line is drawn for visual interpretation but is not indicated in the code. Ground motion was stronger than expected for some frequency bands. D. Detection and forecasting of aftershocks of M>3 using the catalog derived from the whole network (orange) and from a single station (R50D4, blue). Histograms show detections, solid lines show forecast based on fitting an Omori-Utsu law to the first 12 hours of data, with their 95% confidence intervals indicated by dashed lines.

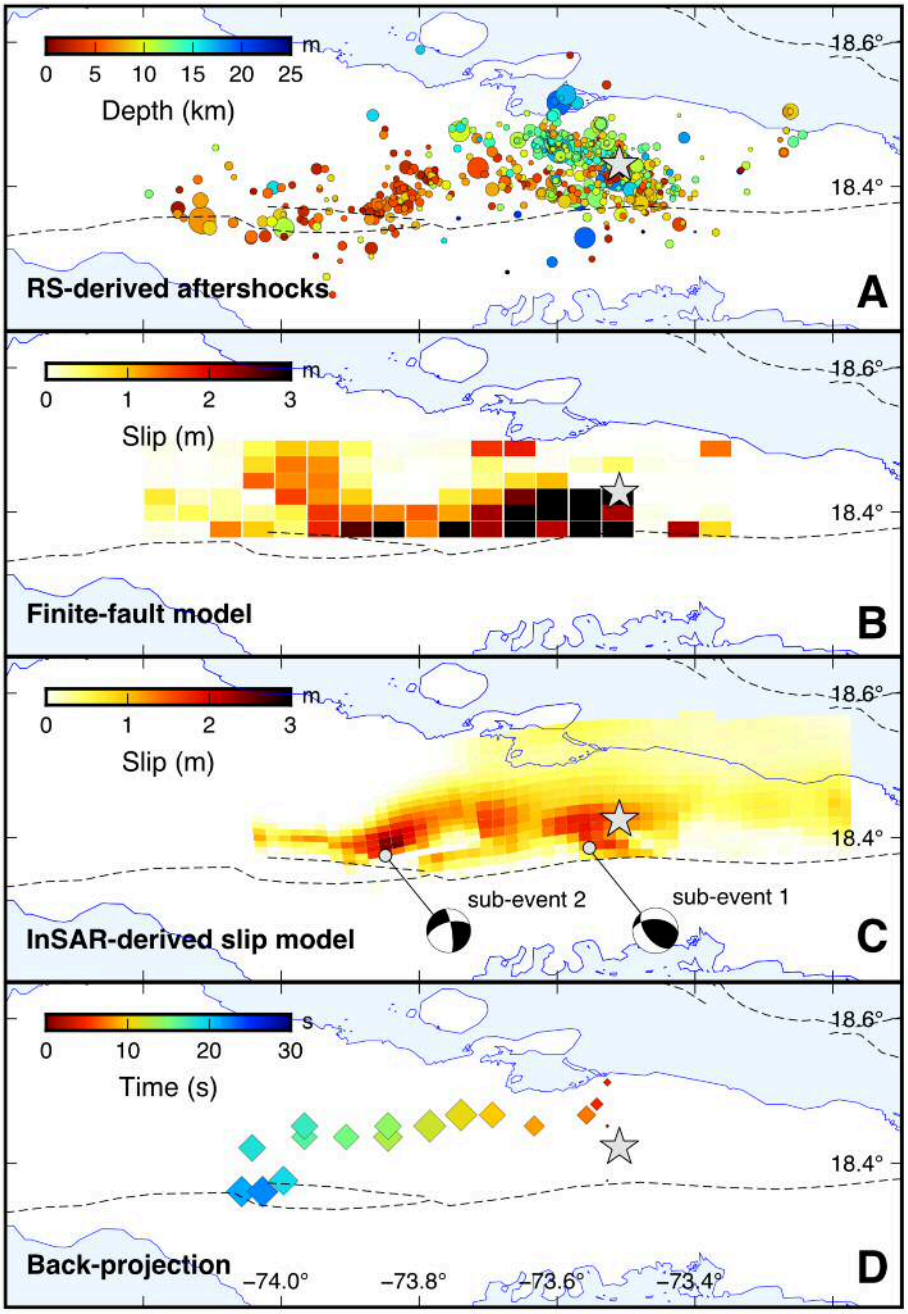

Fig. 3. Comparison between aftershock locations using citizen-hosted seismometers and the mainshock source mechanism. (A) Aftershock catalogue after precise relocation with the 732 higher-quality events (14 August – 9 September 2021). (B) Kinematic finite fault model from an inversion of local and regional seismic stations. (C) Slip distribution inferred from InSAR data. The focal mechanisms derived from long period modelling with two point-sources are shown. (D) High-frequency (1 Hz) radiation sources (diamonds) from teleseismic back-projection source imaging. Symbol size is proportional to their relative energy and colored according to rupture time with respect to the mainshock. The grey star marks the 2021 Nippes epicenter from this study.

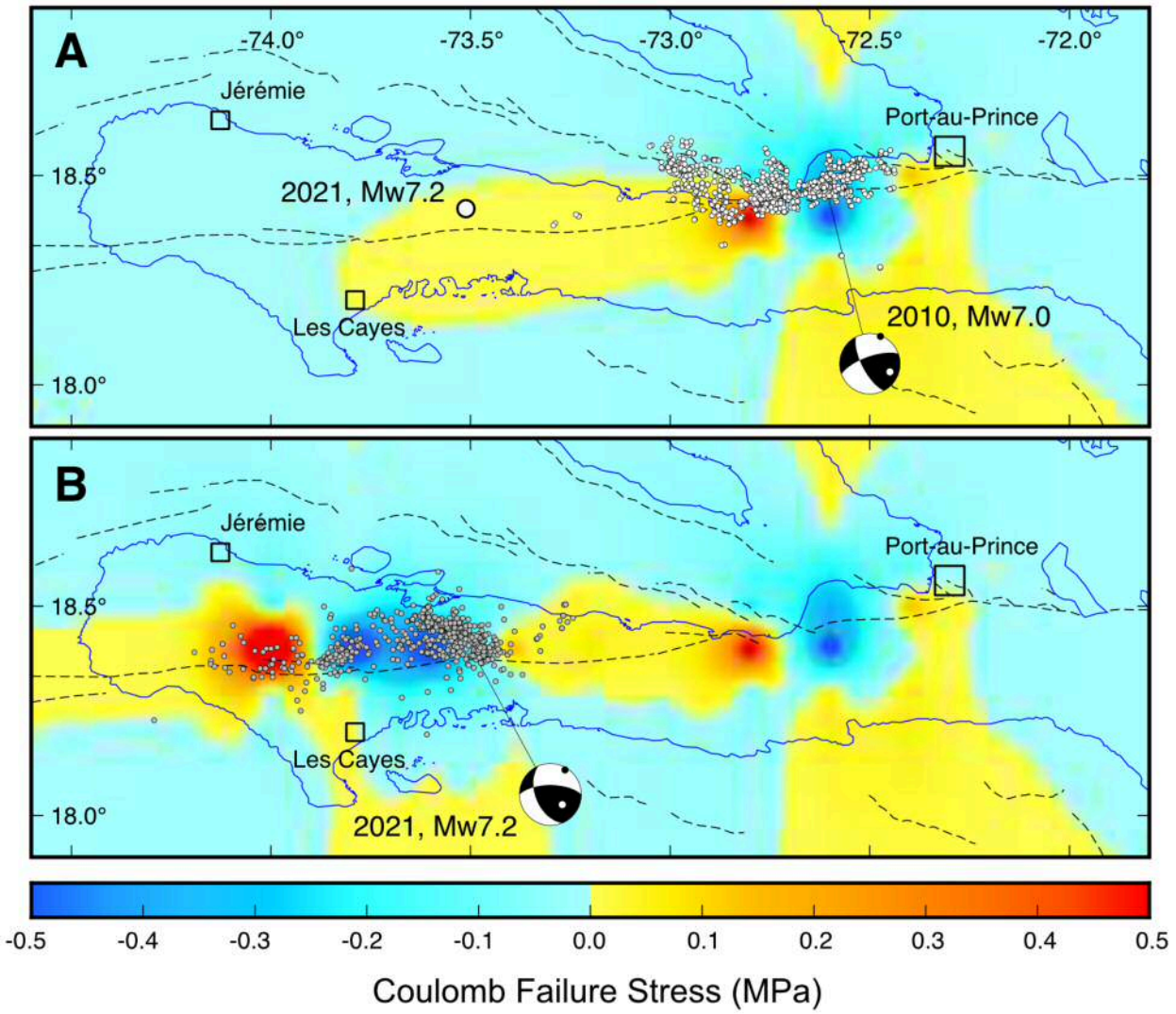

Fig. 4. Coulomb failure stress (CFS) on east-west trending, vertical strike-slip faults. (A) CFS imparted by the 2010 earthquake, with its aftershocks shown as white dots. (B) CFS imparted by both the 2010 and 2021 earthquakes. The grey circles show the 2021 aftershock sequence as of 9 September 2021. CFS is calculated at 5 km depth with a friction coefficient of 0.2.

Materials and Methods

The Materials and Methods used in this work are integrated and detailed in the Supplementary Text below.

Supplementary Text

1. The ayiti-seismes "seismo-citizen" platform

We started deploying Raspberry Shake seismic stations (RS) in Haiti in 2019, equipped with single-component vertical velocimeters and 3-component accelerometers. They are hosted by private individuals who provide internet access and electricity. The stations are located in convenient locations for the hosts (living room, office, etc.), with the consequence that ambient noise can be high. There are currently 15 such stations operating in Haiti. We then developed an automated earthquake detection system, the "ayiti-seismes platform", based on both Seiscomp3 modules *(35)* and software developed at Géoazur, using data from RS seismometers together with low-noise conventional regional permanent seismic stations from surrounding countries such as Cuba and the Dominican Republic. This system outputs earthquake locations and magnitude (Mlv) in real-time through a simple web interface (https://ayiti.unice.fr/ayiti-seismes/). This information is regularly updated (confirmed or rejected) by a seismologist, generating an earthquake catalogue available on the website. Data and metadata are also available from the ayiti-seismes platform through FDSN protocols. Prior to the August 14, 2021, Nippes earthquake, the ayiti-seismes platform provided rapid seismological information for earthquakes of magnitude greater than ~2.5, and events as small as magnitude 1.4–2.0 under certain conditions. Three RS instruments were installed in the epicentral area of the 2021 Nippes earthquake, with one operational at the time of the earthquake. The two inoperative ones – because of internet connection issues – were restored spontaneously within two hours after the mainshock by their hosts. In the epicentral area, we were also able to equip two additional volunteer hosts within 3 days after the event and are receiving additional requests throughout the country.

2. Accelerogram and code response

The response spectrum is a representation that provides a link between seismology and earthquake engineering. It represents an envelope of the peak responses of many single-degree-of-freedom systems over a range of periods. The abscissa of the spectrum is the natural period of the system, the ordinate the maximum acceleration. The response spectrum thus allows us display the impact of the earthquake on very simple buildings assimilated to oscillators. The damping is taken equal to 5% for concrete buildings. Here we compare the elastic response spectrum calculated for the north-south component of RS station R50D4 with the spectrum values indicated in the Haiti National Building Code *(22)* for 5 values (red dots on Figure 2C, main text). We find that the value of the Haitian building code was well adapted for this earthquake at a period zero (PGA value) but slightly too low for higher periods that correspond to buildings of a few floors. As this code was elaborated in 2012 only, it is likely applied to a limited number of buildings in Haiti.

3. FMNEAR waveform inversion

Mainshock:

The FMNEAR method *(36)* inverts the bandpass filtered displacement waveforms of broadband and strong motion records at local to regional distance, searching for the double couple focal mechanism. In the case of large events, like the 2021 Mw7.2 Nippes earthquake, the

source is represented by a linear extended model oriented along fault strike. A series of points sources are aligned in the strike direction of the focal mechanism, on both sides of the hypocenter so that bilateral and unilateral ruptures can be explored. All point sources have the same depth.

The parameter space for the strike, dip, and rake parameters of the focal mechanism is explored in a nonlinear way combining a grid search and a simulated annealing algorithm while the moment magnitude (Mw) is re-evaluated at each step.

Synthetic seismograms are computed using the discrete wavenumber method of *(37)* designed for 1D velocity models. For the 2021 Nippes earthquake, we use a tabular velocity model where the crust is divided into 4 layers with P wave velocity varying from 5.4 at the surface to 6.6 km/s at the base of the crust. The Moho is located at 30 km depth and mantle P wave velocity is 7.9 km/s. The Vp/Vs ratio is 1.75 in the crust and 1.73 in the mantle. This model has been obtained for south-western Haiti from the inversion of travels times of the 2021/04/06 Ml4.6 foreshock and the 2021/08/25 Ml4.5 aftershock of the Nippes earthquake whose locations are well controlled by the local RS stations. We nonetheless carried out the inversion with different velocity models to check that the solution did not vary much according to the velocity model used. The mainshock epicenter is fixed at 18.42°N/73.51°W.

We repeated the inversion for various fixed depth from 1 to 25 km with an increment of 1 km. The retained solution is that minimizing the RMS (Root Mean Square) misfit function of the waveforms, corresponding to a depth of 6 km and [strike, dip, rake] = [265°, 60°, 51°], with a moment magnitude Mw = 7.25. The depth of 6 km should be interpreted as the optimal depth of seismic moment along strike for the whole rupture, not that of the hypocenter itself. The detailed result is presented in Figure S1. Note that the distribution of seismic moment along strike, corresponding to the seismic moment of the point sources distributed on both sides of the hypocenter, indicates that more seismic moment was released to the west, meaning that the rupture propagated essentially westward.

Displacement waveforms are bandpass filtered between 0.01 and 0.05 Hz, except the accelerometric channels of GTBY, NQUS, and RS station R50D4, which are noisier at low frequency and which are filtered in the range 0.02 to 0.05 Hz, 0.02 to 0.05 Hz, and 0.06 to 0.12 Hz, respectively.

Foreshock of 2021/04/06 (05:22 UTC), Ml4.6 and aftershock of 2021/09/25 (10:51 UTC), M_l4.5:

Graphical results of the FMNEAR inversion for the foreshock and the aftershock are presented in Figure S2 and Figure S3. We used the same FMNEAR methodology as for the mainshock, with a single point source. Regarding the specific use of the RS stations, we only used their velocimetric vertical component (EHZ) since the accelerometric 3-component channels are too noisy at low frequency for such moderate size earthquakes. After deconvolution by the instrument response and integration to displacement, these vertical components are bandpass filtered between 0.15 and 0.3 Hz. Regarding the broadband stations, the low- and high-frequency cut-off may vary from one station to the other depending on their signal-to-noise ratio, but are bounded between 0.03 and 0.12 Hz.

<u>Source parameters for the foreshock:</u>
Mw 4.15, epicenter at 18.41°N/73.49°W (fixed), depth 13 km
[strike, dip, rake] = [295°, 80°, 61°] or [187°, 30°, 159°]

<u>Source parameters for the aftershock:</u>

Mw 4.0, epicenter at 18.42°N/73.51°W (fixed), depth 17km
[strike, dip, rake] = [311°, 15°, 86°] or [135°, 75°, 91°]

4. High-precision earthquake relocations with the NLL-SSST-coherence procedure

We obtain high-precision earthquake relocations through the combined use of source-specific, station travel-time corrections (SSST) and stacking of probabilistic event locations based on inter-event waveform coherence. We use the NonLinLoc location algorithm [*(38,39)*; NLL hereafter], which performs efficient, global sampling to obtain an estimate of the posterior probability density function (PDF) in 3D space for hypocenter location. This PDF provides a complete description of likely hypocentral locations with comprehensive uncertainty information, and allows robust application of waveform coherence relocation. Within NLL, we use the equal differential-time likelihood function *(40-43)*, which is highly robust in the presence of outlier data caused by large error in phase identification, measured arrival-times or predicted travel-times. We use a finite-differences, eikonal-equation algorithm *(44)* to calculate gridded P and S travel-times for initial NLL locations. See *(45)* for more details.

Source-specific station term corrections:

In a first relocation stage, NLL-SSST-coherence iteratively develops SSST corrections, which can greatly improve relative location accuracy and clustering of events *(46–49)*. In contrast to station static corrections *(50–52)* which give a unique time correction for each station and phase type, SSST corrections vary smoothly throughout a 3D volume to specify a source-position dependent correction for each station and phase type. Spatial-varying, SSST corrections are most important when the ray paths between stations and events differ greatly across the studied seismicity, including when stations are inside the seismicity distribution, the extent of seismicity is large relative to the distance to the stations, or the depth range of events is large. SSST corrections increase in importance as error in the velocity model increases, such as when a 1D, laterally homogeneous model or a large-wavelength, smooth model is used in an area with sharp, lateral velocity contrasts or small scale, 3D heterogeneity. Within the NonLinLoc package, SSST corrections are developed iteratively with spatial smoothing of decreasing size using a Gaussian kernel, this approach is similar to the shrinking box SSST approach of *(48)*. See *(45)* for more details.

Waveform coherency relocation method:

In a second relocation stage, NLL-SSST-coherence invokes a recently developed procedure *(45)* which greatly reduces aleatoric location error by consolidating information across event locations based on waveform coherency between the events. This coherency relocation, NLL-coherence, is based on the concept that if the waveforms at a station for two events are very similar (e.g., have high coherency) up to a given dominant frequency, then the distance separating these events is small relative to the seismic wavelength at that frequency *(53,54)*, perhaps less than about ¼ of this wavelength *(53,55)*. A pair of similar events is a doublet and a set of similar events may be called a cluster, multiplet or family, these events all likely occur on a small patch of a fault with similar magnitude and source mechanism *(53, 54,56–59)*. In a high-precision microseismic study, *(60)* show for waveform windows spanning both P and S waves that correlation coefficients greater than about 0.7 indicate event multiplets locate within about 0.1 km, which is about ¼ wavelength for the typical dominant waveform frequency of ~20 Hz and wave velocity of ~2.5 km/s shown in their study. The results of *(60)* also show lack of clustering and separation of event pairs throughout the region of studied seismicity for correlation coefficients less than about 0.5 (their figs. 4 and 6).

For detailed seismicity analysis, the precise hypocenter locations of events in multiplets can be assigned to a unique centroid point or coalesced in space through some statistical combination of the initial hypocenter locations *(61,62)*. Alternatively, precise, differential times between like-phases (e.g., P and S) for doublet events can be measured using time- or frequency-domain, waveform correlation methods. Differential times from a sufficient number of stations for pairs of doublet events allows high-precision, relative location between the events, usually maintaining the initial centroid of the event positions *(54, 59, 63–68)*.

Here we use waveform similarity directly to improve relative location accuracy without the need for differential time measurements or many stations with waveform data. We assume that high coherency between waveforms for two events implies the events are nearly co-located, and also that all of the information in the event locations, when corrected for true origin-time shifts, should be nearly identical in the absence of noise. Then, stacking procedures can be used to reduce the noise in this information and improve the location precision for individual, target events. We use the coherency between waveforms for pairs of events (i.e., the target event and all other events) at one or more stations to combine through stacking an initial set of NLL location probability density functions (PDF's). This stack directly improves the hypocenter location for each target event by effectively combining and completing arrival time data over events and reducing noise (aleatoric error) in this data.

For an event that has low coherency with all other events, the PDF stack and all location information will be identical to those for the initial location for the event. For an initial event that is poorly constrained with an extensive PDF, but which has high coherency with other, well constrained events, the stacked PDF location will closely match the locations of the well constrained events. Unlike differential-time based, relative location methods, NLL-coherence relocation can be performed with waveforms from few or even a single station. Consequently, NLL-coherence relocation is computationally efficient, allows precise relocation of seismicity when the closest station is far from the seismicity and for sparse networks, enables precise relocation of foreshocks and early aftershocks in a mainshock sequence or swarm before nearby temporary stations are installed, and can be applied to historical sequences with little available waveform data.

Application to the 2021 Nippes, Haiti sequence

We obtain a catalogue of all available events (1125 events) including P and S arrival times for the southwestern Haiti area (latitude 17.7° to 19.1°, longitude -74.6° to -73.0°) with $M \geq 1.5$ from 2020-08-14 to 2021-09-09 from the Ayiti-Seismes Project FDSN webservice (https://ayiti.unice.fr/ayiti-seismes/fdsnws). Because it does not use near-field, RS stations, the USGS database contains only 37 events for the same time interval, all of magnitude greater than 3.8 (ranging between 3.8 and 5.8, see https://earthquake.usgs.gov). We obtain waveforms for the catalog events for selected stations to use for NLL-SSST-coherence relocation from the FDSN webservices at https://fdsnws.raspberryshakedata.com and http://service.iris.edu.

For initial NLL location we use the 1D, "Ayiti01" P and S velocity profile (Figure S4) which is based on an optimal model obtained for the SlipNear inversions in this study, combined with information from the minimum 1D model of *(69)*, and below 77.5 km the IASP91 model *(70)*.

For the 2021 Nippes, Haiti NLL-SSST relocations, we iteratively generating SSST corrections using the Ayiti-Seismes Project catalogue events and arrival data with smoothing distances, D, of 64, 32, 16, and 8 km. The quality criteria for an event location and station-phase to be included for calculating SSST corrections are: 68% error-ellipsoid principle-axis half-width

≤ 10.0 km, root mean square of residuals (rms) ≤ 0.5 s, number of readings ≥ 10, azimuth gap ≤ 150°, P residual ≤ 1.0 s, S residual ≤ 2.0 s.

For the 2021 Nippes, Haiti NLL-coherence relocations, we measure coherency using waveforms from vertical component channels from four nearby stations over and around the main seismicity: AM.R1719.00.EHZ, AM.R50D4.00.EHZ, AM.RCE1F.00.EHZ, CN.LGNH.HHZ, CW.MASC.00.HHZ, CW.QMBU.00.HHZ. The waveforms are filtered from 1-5 Hz in a window from 4 seconds before the predicted P arrival to 4 seconds after the predicted S arrival. Cross-correlation is applied between waveforms windows sliding from -2.0 to 2.0 sec, and a 0-1 stacking weight is set over coherency values from Cmin = 0.5 to 1.0. This procedure is applied to the D = 8 km NLL-SSST relocations for all event pairs with a maximum hypocenter separation of 5.0 km. 633 final NLL-SSST-coherence relocations (foreshocks and aftershocks) filtered with 68% error-ellipsoid principle-axis half-width < 20.0 km and hypocenter depth > 1 km are shown in the main paper (Figure 1A and 3A) and are available as a CSV format table in DataSet S1. Various location statistics for this set of locations is shown in Figure S5. Histograms of formal epicentral errors (errH) for the initial NLL locations allow an estimate of absolute epicenter errors of up to 5-8 km for better constrained events. Histograms of formal epicentral errors (errH) for the final NLL-SSST-coherence locations (Figure S5) suggest an estimate of relative error between nearby epicenters constrained by waveform similarity to be as low as 2-3 km.

5. Aftershock forecasts

We forecast the evolution of the daily rate of aftershocks by applying the method of Reasenberg and Jones *(25,71)*, which relies on two robust empirical relations of statistical seismology, the Gutenberg-Richter law of magnitude distribution and the Omori-Utsu law of aftershock rate decay, and does not account for secondary aftershocks (aftershocks of aftershocks). We fix the value of the exponents b=1 and p=1, and compute the Maximum-Likelihood estimates of productivity K and time scale c *(72)*. The 90% confidence intervals of the daily rates are evaluated assuming a non-stationary Poisson process.

We apply this forecasting technique to wo independent data sets:

1. The aftershock catalog derived from ayiti-seismes network analysis, described above.
2. An aftershock catalog derived from recordings of a single RS station located close to the earthquake rupture (R50D4). To do to, we trained a Machine Learning algorithm to detect earthquakes of magnitude > 3 using a training database composed of earthquake and noise data from the STEAD database *(73)* and the Peruvian National Seismic Network (IGP), augmented by noise recorded by station RS50D4. Using an Extreme Gradient Boosting algorithm *(74)* we find the best combinations of 54 attributes per channel, from temporal, spectral and cepstral domains, that classify noise and P wave signals. We applied this detector to data from the vertical geophone of station RS504D.

6. Kinematic slip inversion using regional seismological data

The detail of the kinematic inversion is shown in Figure S7. The slip inversion methodology used here was initially developed for the 1999 Izmit earthquake *(75)*. It shares similarities with the FMNEAR inversion described above, but here point sources are distributed on a rectangular fault model whose strike (270°) and dip (60°) are fixed according to the FMNEAR focal mechanism and to the average orientation of the Enriquillo fault trace. The mainshock epicenter is fixed at 18.42°N/73.51°W and fault dip imposes a rupture initiation at 11 km depth,

intermediate between the depth found by travel time inversion (19 km) and by the FMNEAR linear source inversion (6 km).

Final model length (90 km) and width (30 km), as well as the number of equally spaced point sources used to discretize the rupture (108 in total), are optimized after a series of initial inversions. Rupture dimensions are large enough to encompass all the significant slip areas required by the data. The model is much longer towards the west since initial models reaching further east showed almost no slip to the east of the hypocenter. The dominant westward rupture propagation already suggested by the FMNEAR inversion is confirmed by the rectangular fault model inversion. A local moment rate source time function is associated with each point source, discretized by a series of three mutually overlapping isosceles triangles. The onset time of each point source, the rake angle, and the amplitudes of the triangular elements are inverted for using a simulated annealing algorithm. Rupture onset times of the point sources are bracketed using two bounding rupture velocities, 1.5 and 4.0 km/s. The slip angle (rake) may vary by +/- 50° around a central value of 50° (reverse – left lateral). The fault model reaches the earth surface at its top—southern limit

The criterion to assess the quality of the solution is the minimization of the normalized root mean square (RMS) misfit error on the waveforms, with a constraint to minimize the total seismic moment. It also incorporates smoothing functions on the slip, rupture velocity, and rake parameters. Additionally, we explored different constraints on the maximum allowed slip value. All these constraints help stabilize the inversion but trade-off with the RMS misfit function (the stronger the constraint, the larger the RMS). The solution presented here is a compromise with respect to these trade-offs.

Considering that we want to obtain a more detailed image of the rupture process, displacement waveforms are bandpass filtered with a slightly higher maximum frequency than in the FMNEAR inversion. Synthetic seismograms are computed using the discrete wavenumber method of *(37)* designed for 1D velocity models. The tabular velocity model used is the same as for FMNEAR, with a Vp/Vp ratio adjusted to 1.71 in the crust and in the mantle for some stations in Cuba which displayed delays in arrival times for the S and surface waves train.

Graphical results of the kinematic source inversion are shown on Figure S6. The resulting moment magnitude is Mw 7.24.

7. <u>High-frequency rupture imaging by teleseismic back-projection</u>

We image the high-frequency components of the mainshock rupture by teleseismic back-projection. This technique provides the space-time distribution of high-frequency radiation sources along the rupture, without resolving their source depth. Back-projection relies solely on the relative arrival times across the array, and does not involve restrictive assumptions about fault geometry and rupture kinematics. We apply the high-resolution Multitaper-MUSIC back-projection method with reference window correction and Slowness-Enhanced calibration *(76-78)*. The analysis is usually performed on coherent seismograms recorded by dense arrays at teleseismic distances from the epicenter (30°-90°). Here, we use P-wave seismograms recorded by 215 broadband stations distributed across Alaska (Figure S8), with epicentral distances between 57° and 82°, whose data is available from the IRIS data center. The data is filtered in the 0.25-1 Hz frequency band. The analysis is done on sliding windows of duration 10 s.

In conventional back-projection, P-wave travel times are calculated with a 1-D reference velocity model (for example, IASP91). Travel time errors due to 3-D path effects result in a spatial bias of the subevent locations imaged by back-projection. In the vicinity of the hypocenter, these errors are mitigated by pre-aligning the waveforms on their first P-wave arrival, which effectively applies station-dependent hypocentral travel time corrections. Away

from the hypocenter, the Slowness-Enhanced Back-Projection method *(78)* estimates corrections for the spatial derivatives of travel time in the source area derived from aftershock data, which effectively applies a slowness correction over the rupture area. Here, we used three M4.7+ aftershocks from our high-precision relocated catalogue (Figure S8).

8. Radar interferogram processing

Radar interferograms are shown in Figure S9, Figure S10, Figure S11, and Figure S12. We processed the Sentinel 1A and 1B Radar data to form coseismic interferograms using the ISCE processing chain (JPL/CalTech) *(79)*. On the ascending track, we use data acquired on August 5th and August 17th 2021. On the descending track, we use data acquired on August 3rd and August 15th, 2021. We applied two-pass differential interferometry with the hole-filled SRTM digital elevation model *(80)*. SLCs coregistration is performed using orbital information and refined in azimuth using the spectral diversity on burst overlap regions *(81)*. Interferograms are computed on a burst-by-burst approach, then stitched, multilooked (12 looks in azimuth and 48 looks in range), filtered *(82)* and unwrapped using a minimum cost-flow approach [SNAPHU, *(83)*]. We mask pixels with a coherence of less than 0.35.

The ALOS-2 data were provided by the Japan Aerospace Exploration Agency (JAXA) through the Earthquake Working Group for the Evaluation of ALOS and ALOS-2 for Use in Disaster Mitigation, coordinated by the Geospatial Information Authority of Japan (GSI) and JAXA. JAXA conducted emergency observations immediately after the earthquake. We chose acquisitions on December 23rd, 2020 and August 18th, 2021 for the strip map data acquired along an ascending track and acquisitions on December 10th, 2019 and August 17th, 2021 for the wide-swath data acquired along a descending track. We applied two-pass differential interferometry to the ALOS-2 data using the RINC software *(84)* with the digital ellipsoidal height models created from the hole-filled SRTM digital elevation models *(85)* and the EGM96 geoid model *(86)*. The decorrelated noise was suppressed by taking multilook with a window size of 8 x 15 (fine-beam mode) and 8 x 36 (wide-swath mode) in range and azimuth directions, corresponding to approximately 50 x 50 m and 110 x 110 m pixel intervals, and applying a spectral filter *(87)*. The interferograms were unwrapped using the SNAPHU software *(83)* version 2.0.3. Considering the consistency between interferograms we mask pixels with a coherence lower than 0.05 on the fine-beam mode data (ascending track showing surface breaks) and pixels with a coherence lower than 0.13 on the wide-swath data (long temporal baseline).

While both ascending interferograms show motion toward the satellite from the epicentral region to the westernmost end of the rupture, descending interferograms show motion toward the satellite in the epicentral region and away from the satellite along the western part of the rupture. Such reversal of the sense of motion along the LOS direction indicates significant vertical motion in the epicentral region while almost pure horizontal, left-lateral motion is observed to the west. In addition, the coherence of the ALOS2 strip-map data on ascending track shows the rupture reached the surface along the left-lateral strike-slip fault Ravine du Sud fault. No significant surface breaks can be seen on these interferograms and the surface deformation gradients indicates that most of the rupture remained blind otherwise.

9. Non-linear inversion for a 2-fault geometry

We used the CSI package *(88,89)* to derive the most plausible 2-fault geometry that fits the InSAR coseismic displacement field. We solve for the location (longitude, latitude and depth), the orientation (strike and dip angles) and the size (length and width) of 2 rectangular dislocations embedded in an elastic half space simultaneously with the dip and strike slip motion

(90). We down-sampled the interferograms using quadtree approach in which the size of square averaging windows exponentially decays with the distance to the Enriquillo fault.

We used the SLSQP (standard least squares procedure) implementation of SciPy *(93)* to minimize the unregularized least-squares cost-function defined as $S(m) = (g(m) - d)^T C_d^{-1}(g(m) - d)$ where m is the model parameter vector that includes the dislocation geometry parameters and slip values, g is a function building a prediction of the data d and C_d is the data covariance matrix. We build the data covariance matrix by evaluating the noise covariance on the unwrapped interferograms). Diagonal of the data covariance is the variance of the data in regions not affected by coseismic motion. Details of the best-fit solution are shown in Figure *S13* and Figure S14. Model performance is displayed on Figure S15, Figure S16, Figure S17Figure S17, and Figure S18.

10. Linear slip inversion

We used the CSI package *(88,89)* to derive the coseismic slip distribution from the InSAR data (Figure S23, Figure S24, Figure S25, Figure S26). We build our fault geometry considering that the mapped traces of the Ravine du Sud and Enriquillo faults are the surface expressions of the fault we recovered in the non-linear search. We used the inferred dip angle to extend these two faults from their surface trace to depth and then mesh the corresponding surfaces with triangular elements using the python implementation of "distmesh" *(91)*. Triangles have a 2 km side length at the surface and their size increases with depth by a tenth of the depth. We defined slip on the faults as a linear interpolation between nodes over the fault mesh. We built Green's functions assuming a stratified elastic half space based on previous seismological study of the region *(69,92)*. We solve for strike slip and thrust motion on each fault. We evaluate potential orbital and long wavelength signals not related to the earthquake by estimating a range and azimuth ramp in each of the 4 interferograms we use. We down-sampled the interferograms using quadtree approach in which the size of square averaging windows exponentially decays with the distance to the Enriquillo fault.

We used the SLSQP method implemented in Scipy *(93)* to minimize the least-squares cost-function defined as $S(m) = (Gm - d)^T C_d^{-1}(Gm - d) + (m_p - m)^T C_m^{-1}(m_p - m)$ where m is the model parameter vector containing the slip values and the long wavelength ramp parameters, G is the corresponding Green's functions operator, d is the data vector that includes the down-sampled InSAR data, C_d is the corresponding data covariance matrix, m_p is the prior model (here set to the null vector) and C_m is the model covariance matrix. While the first term of the cost-function evaluates the data residuals, the second term regularizes the ill-posed inverse problem. We build the model covariance matrix assuming a covariance between slip on each node that decays exponentially with the distance between nodes *(94)*. We explore values of characteristic distance and variance (i.e., diagonal of the covariance) to find a compromise between mode misfit to the data and model roughness.

11. Multiple point source inversion

We used a multiple point source inversion approach similar to that of *(95)* where multiple double-couple sources are inverted simultaneously using long-period seismic waveforms. Here, we used a time window incorporating body-waves and surface waves bandpass filtered in the period range of 120-500 s. To mitigate biases due to unaccounted lateral heterogeneities, we use Green's functions computed for the 3D Earth model S40RTS *(96)* using the spectral element code SPECFEM3D_GLOBE *(97)*. Point source locations were fixed from the location of faults derived from the non-linear inversion of the two-fault geometry described above. We derived the posterior distribution of double-couple parameters (strike, dip, rake, scalar moment) and centroid

time of each subevent using the Bayesian sampling approach described in *(95)*. Results and data fitting are shown in Figure S19, Figure S20, Figure S21, and Figure S22.

	Time-shift	Strike	Dip	Rake	Mo/1e27 dyne-cm	Mw
Sub-event 1	10 s	273°	48°	52°	0.511	7.07
Sub-event 2	14 s	254°	59°	-14°	0.200	6.80
Composite	11 s	265°	50°	34°	0.639	7.14

Table S1. Posterior mean of the two-point source solution obtained from the inversion of Long-period data. Centroid time-shifts are defined relative to 2021/08/14 12:29:09.40 UTC

12. Coulomb stress modelling

Coseismic fault slip causes changes to the stress field in the surrounding crust that may influence the state of stress along neighboring faults, possibly causing advances or delays in the timing of future events. This process is quantified by changes of the Coulomb failure stress (CFS), the combination of the shear stress that drives a neighboring fault to fail and of the normal (or clamping) stress that keeps it from sliding. The change in CFS on a given receiver fault, defined by its strike, dip, and rake, caused by a nearby earthquake is given by $\Delta\sigma\tau=\Delta\tau-\mu\times\Delta\sigma n$, where $\Delta\tau$ is the change in shear stress, $\Delta\sigma n$ the change in normal stress, and μ the apparent friction coefficient, which accounts for the effect of pore fluid pressure that works to reduce friction. A positive $\Delta\sigma\tau$ corresponds to a receiver fault being brought closer to failure, whereas a negative change corresponds to failure being delayed *(98,99)*. Regions of positive $\Delta\sigma\tau$ have been shown to coincide with the location of aftershocks, as well as the initiation of several large earthquake sequences. The calculation uses rupture geometries and coseismic slip from the finite fault model computed by *(25)* for the 2010 earthquake, and the InSAR-derived one for the 2021 event (Figure 3). The calculation uses the formalism of screw dislocations on faults embedded in an isotropic elastic half-space with calculated Green's functions from *(90)*. The resulting coseismic stresses are projected onto components that are perpendicular and parallel to the rake of each segment of the receiver faults to calculate the corresponding $\Delta\sigma\tau$.

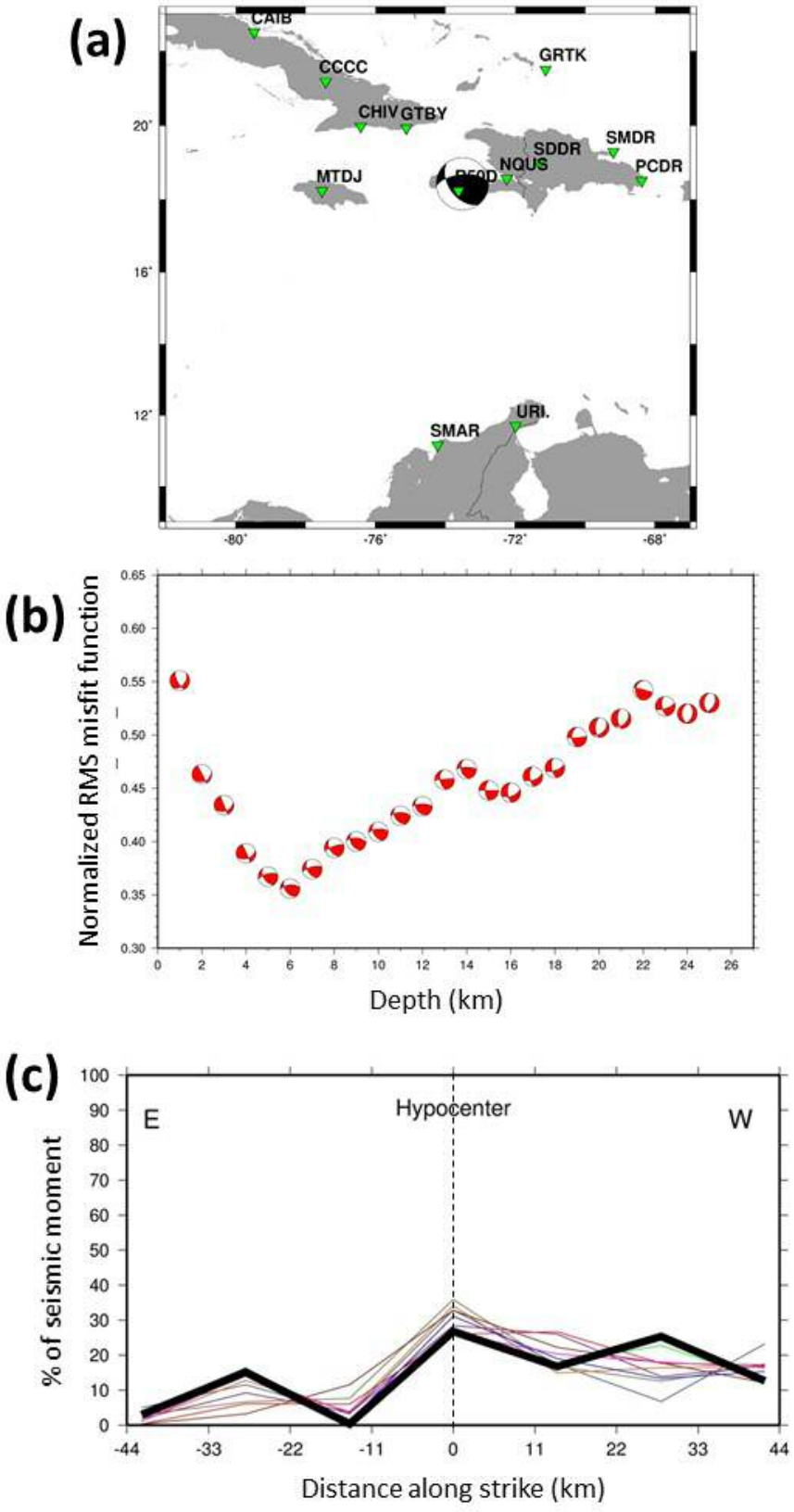
(a)
CAIB
CCCC
GRTK
CHIV
GTBY
SMDR
SDDR
NQUS
PCDR
MTDJ
URI.
SMAR
20°
16°
12°
-80°
-76°
-72°
-68°
(b)
Normalized RMS misfit function
0.65
0.60
0.55
0.50
0.45
0.40
0.35
0.30
0
2
4
6
8
10
12
14
16
18
20
22
24
26
Depth (km)
(c)
% of seismic moment
100
90
80
70
60
50
40
30
20
10
0
E
Hypocenter
W
-44
-33
-22
-11
0
11
22
33
44
Distance along strike (km)

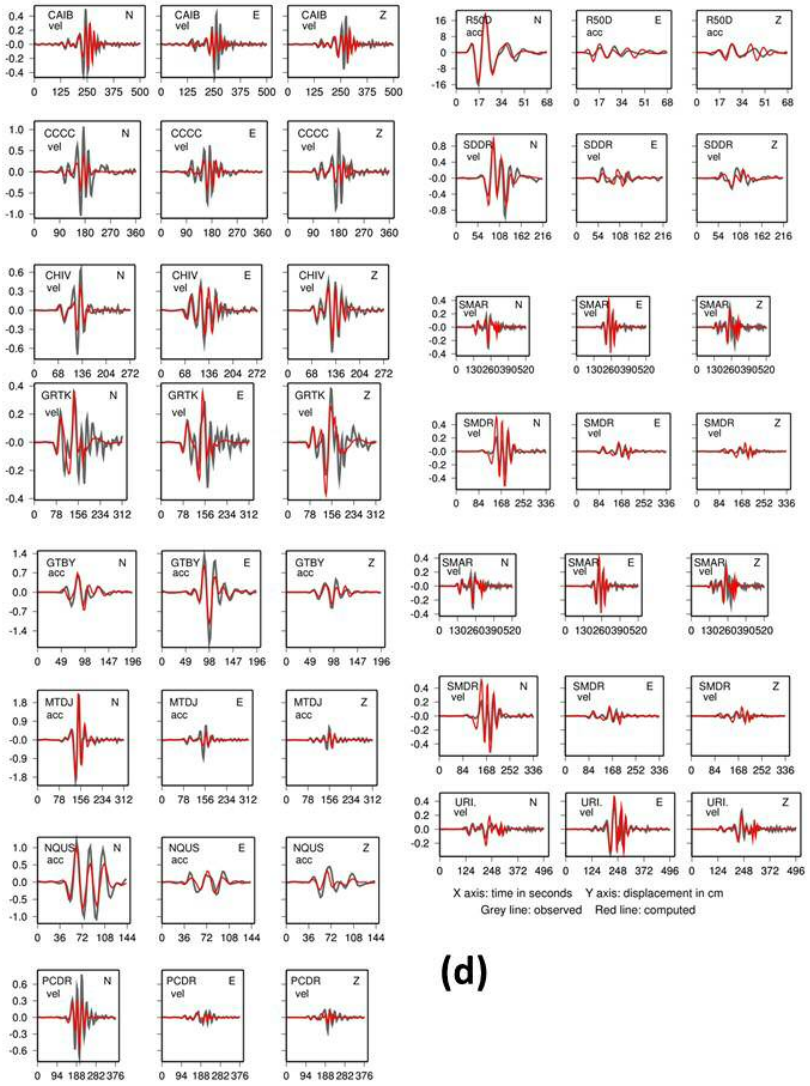

Figure S1. Result of the FMNEAR inversion for the 2021 Mw7.2 Nippes earthquake. (a) Map of stations used (green triangles), with the best solution for the focal mechanism (FM) at its epicentral location. (b) FM solutions as a function of depth and normalized RMS misfit function. The best solution is found at a depth of 6 km. (c) Distribution of seismic moment, in percentage, along strike, resulting from the FMNEAR inversion using a linear finite source model. The hypocenter is located at distance = 0 (vertical dashed line) and distance in km is measured positive westward and negative eastward. All curves, corresponding to 10 different inversions, show larger % values of seismic moment release in the West. (d) Waveform fit, in displacement (cm) bandpass filtered (see text). Observed records are in grey and computed in red. For each station the three components are displayed (N, E, Z), and 'vel' or 'acc' means that the original record was in velocity (broadband) or in acceleration (strong motion), respectively. Station names may be truncated if they contain more than four letters.

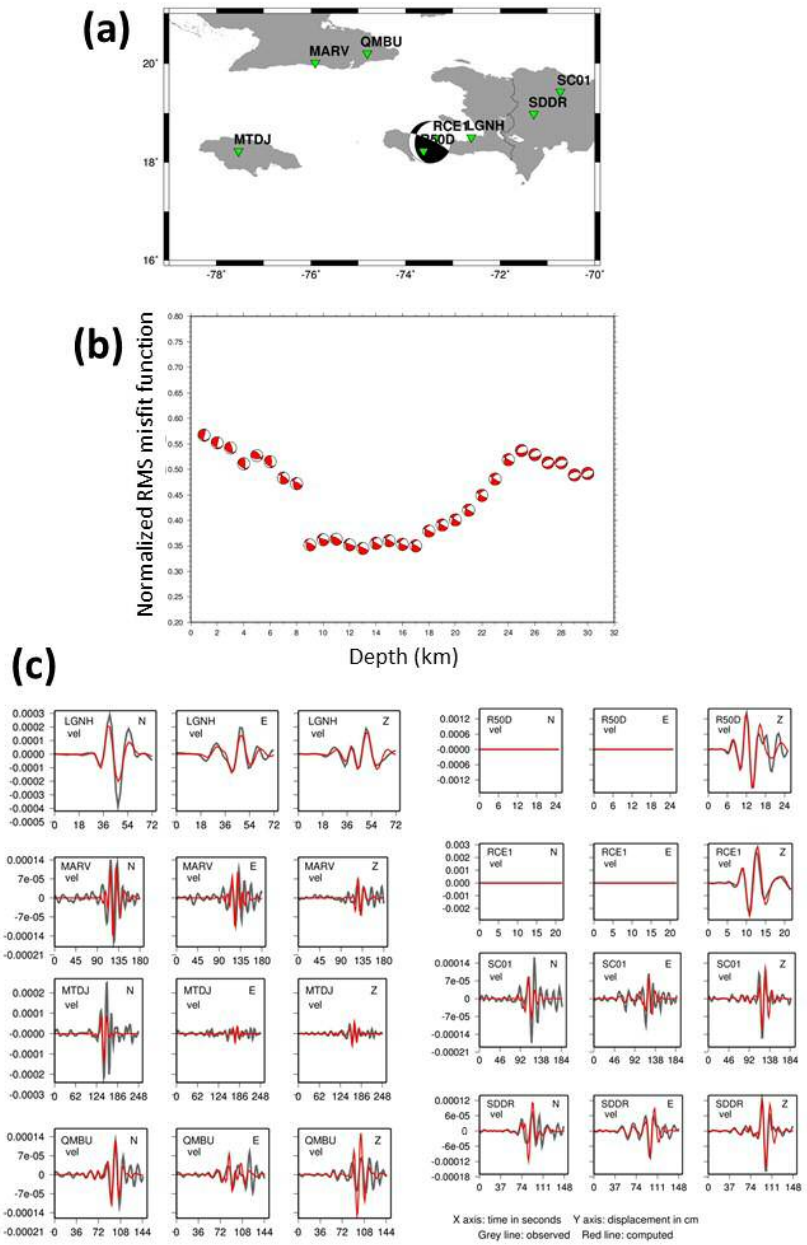

Figure S2. Result of the FMNEAR inversion for the 2021/04/06 Ml4.6 foreshock. (a) Map of stations used (green triangles), with the best solution for the focal mechanism (FM) at its epicentral location. (b) FM solutions as a function of depth and normalized RMS misfit function. The best solution is found at a depth of 13 km, but similar quality solutions are found between 8 and 17km depth. (c) Waveform fit, in displacement (cm) bandpass filtered (see text). Observed records are in gray and computed in red. For each station the three components are displayed (N, E, Z), and 'vel' or 'acc' means that the original record was in velocity (broadband) or in acceleration (strong motion), respectively. Station names may be truncated if they contain more than four letters. In the case of RS stations R50D4 and RCE1F, only the vertical (Z) component is used, and the N and E velocimetric components, not existing, are shown as flat.

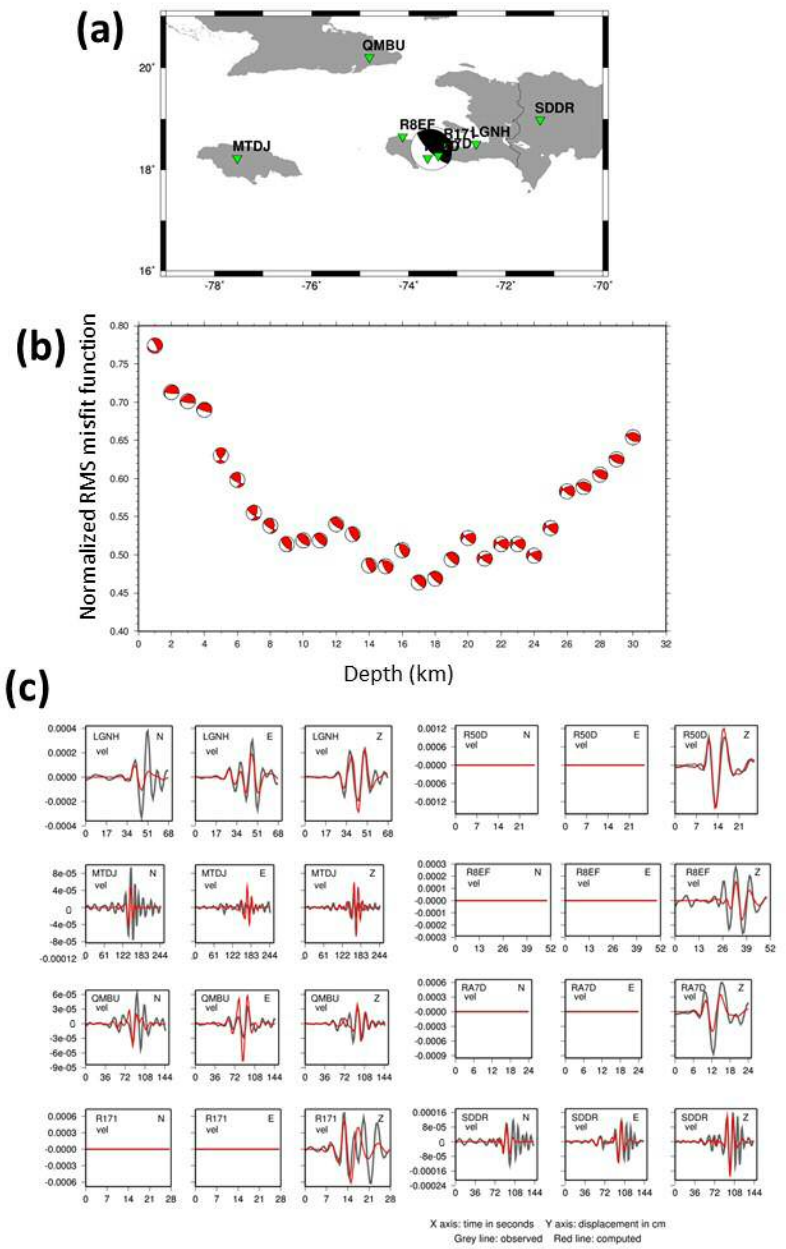

Figure S3. Result of the FMNEAR inversion for the 2021/08/25 Ml4.5 aftershock. (a) Map of stations used (green triangles), with the best solution for the focal mechanism (FM) at its epicentral location. (b) FM solutions as a function of depth and normalized RMS misfit function. The best solution is found at a depth of 17 km. (c) Waveform fit, in displacement (cm) bandpass filtered (see text). Observed records are in gray and computed in red. For each station the three components are displayed (N, E, Z), and 'vel' or 'acc' means that the original record was in velocity (broadband) or in acceleration (strong motion), respectively. Station names may be truncated if they contain more than four letters. In the case of RS stations R1719, R50D4, R8EFE, and RA7D0, only the vertical (Z) component is used, and the N and E velocimetric components, not existing, are shown as flat.

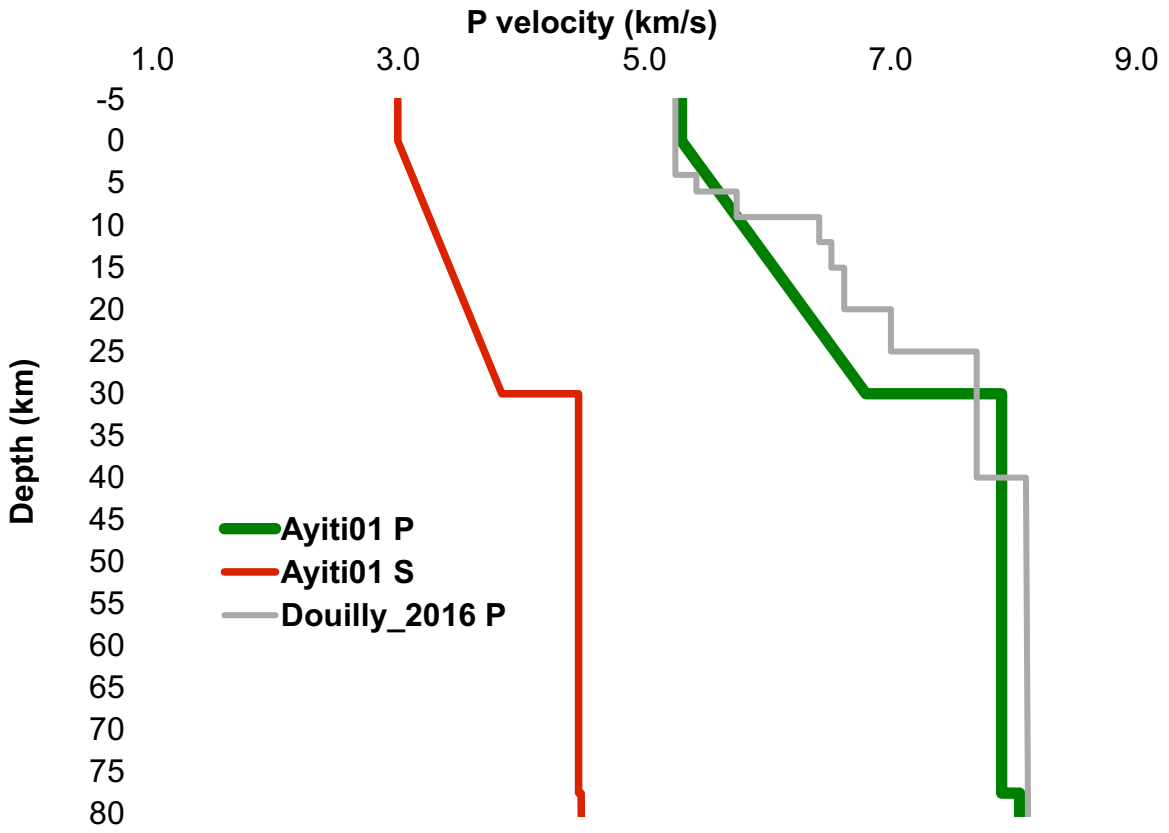

Figure S4. 1D Ayiti01 P and S velocity models used for initial NLL location and minimum 1D P model of Douilly et al. (2016).

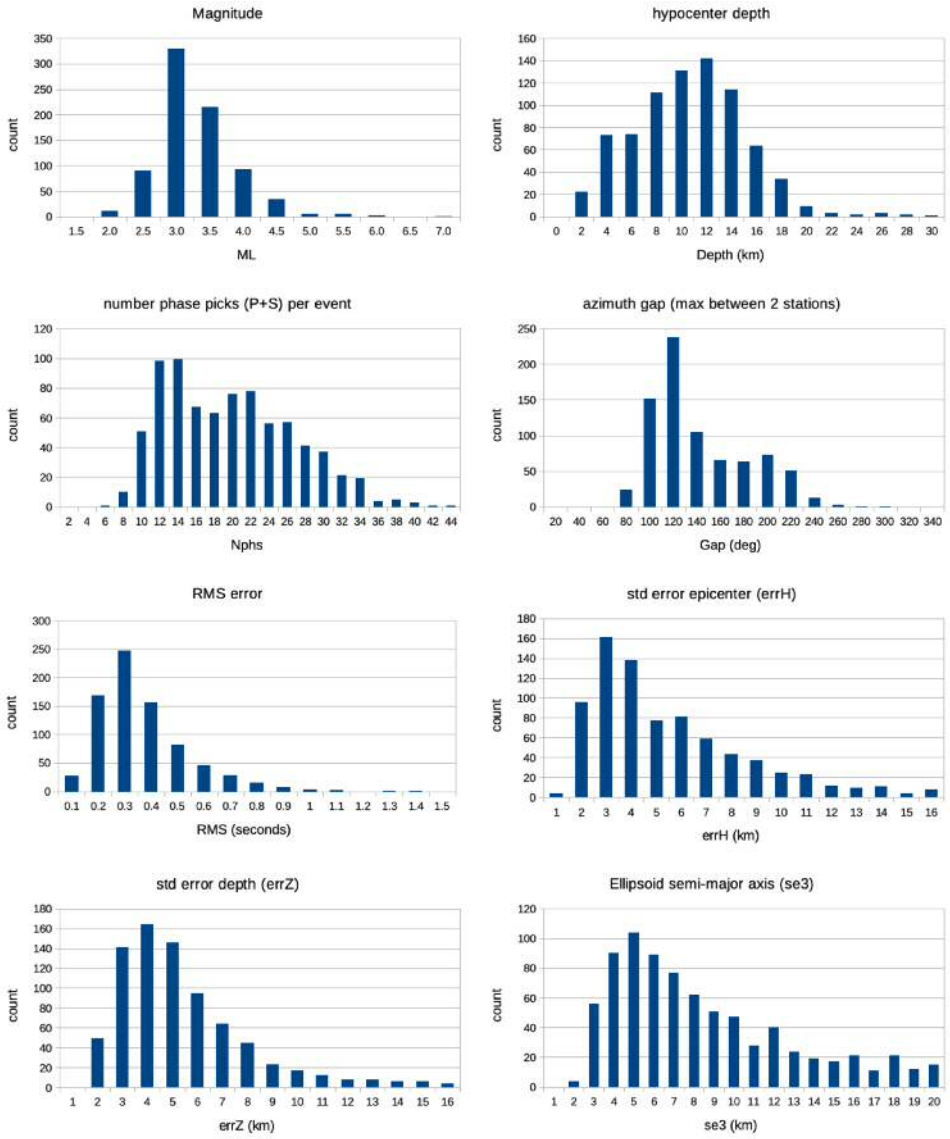

Figure S5. Histograms of various location statistics for 788 final NLL-SSST-coherence relocations (foreshocks and aftershocks) filtered with 68% error-ellipsoid principle-axis half-width ≤20.0 km and hypocentre depth ≥1 km.

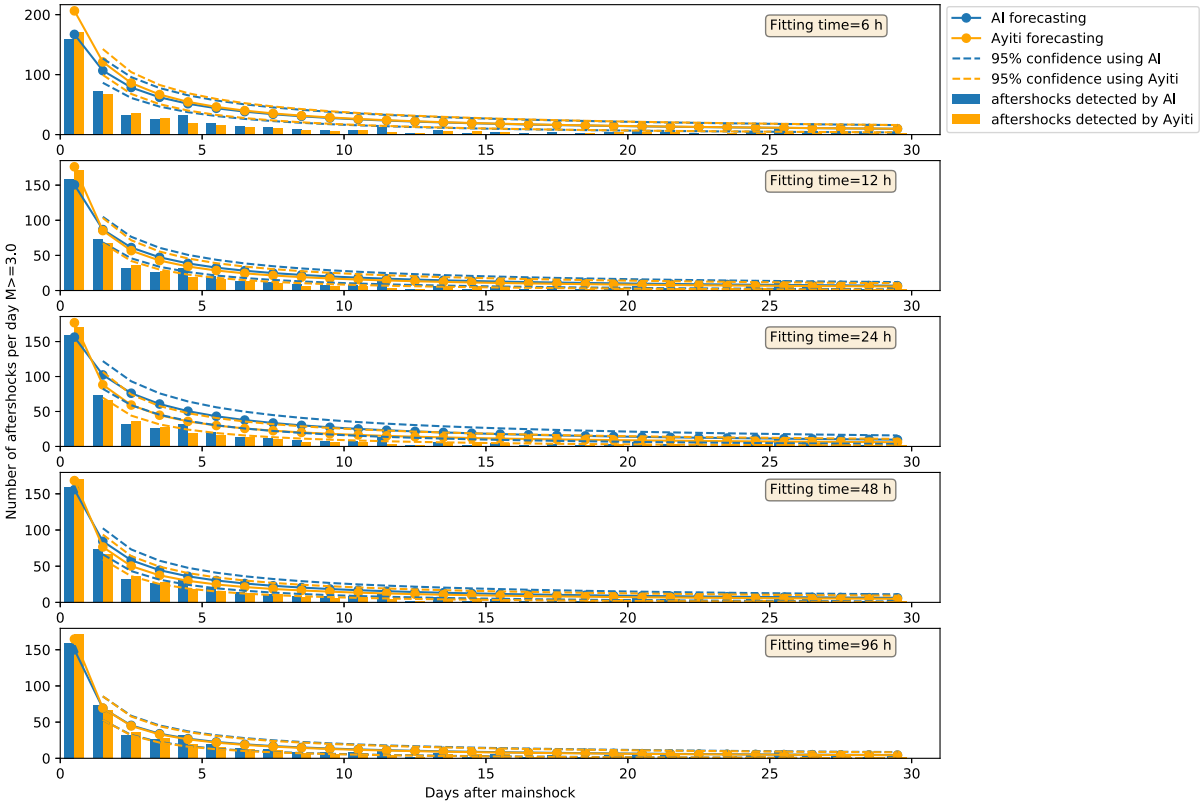

Figure S6. Daily aftershock rate forecast for events of magnitude larger than 3 inferred from 5 different forecasting windows: 6, 12, 24, 48, and 96 hours after the mainshock. Histograms show detections (AI = machine learning algorithm based in a single RS station (R50D4), ayiti = forecast using the network-derived catalog), solid lines show forecast based on fitting an Omori-Utsu law, with the 95% confidence intervals indicated by dashed lines

.

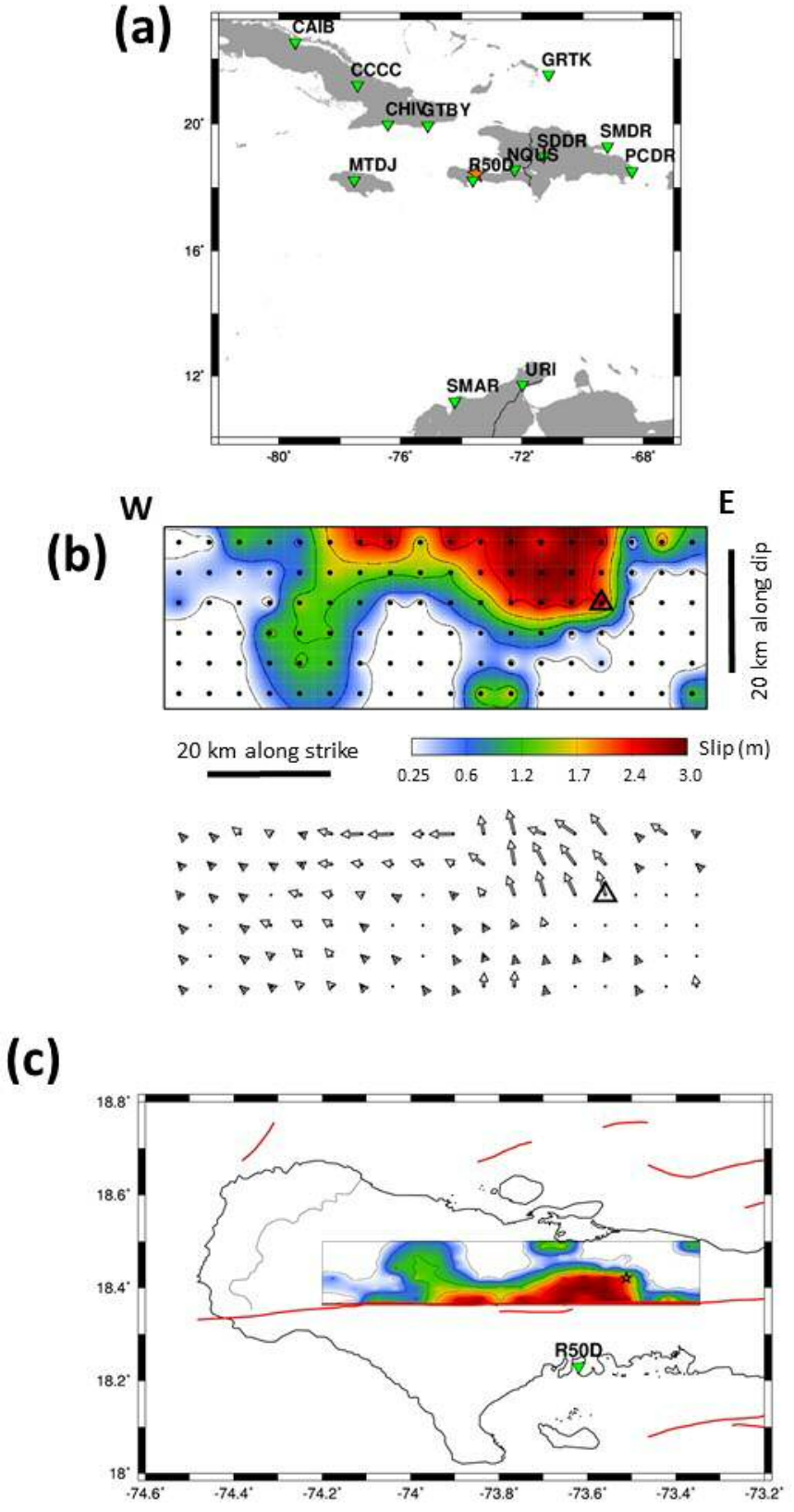
(a)
CAIB
CCCC
GRTK
CHIV
GTBY
SDDR
SMDR
NQUS
PCDR
MTDJ
R50D
SMAR
URI
20°
16°
12°
-80°
-76°
-72°
-68°
(b)
W
E
20 km along dip
20 km along strike
Slip (m)
0.25 0.6 1.2 1.7 2.4 3.0
(c)
R50D
18.8°
18.6°
18.4°
18.2°
18°
-74.6°
-74.4°
-74.2°
-74°
-73.8°
-73.6°
-73.4°
-73.2°

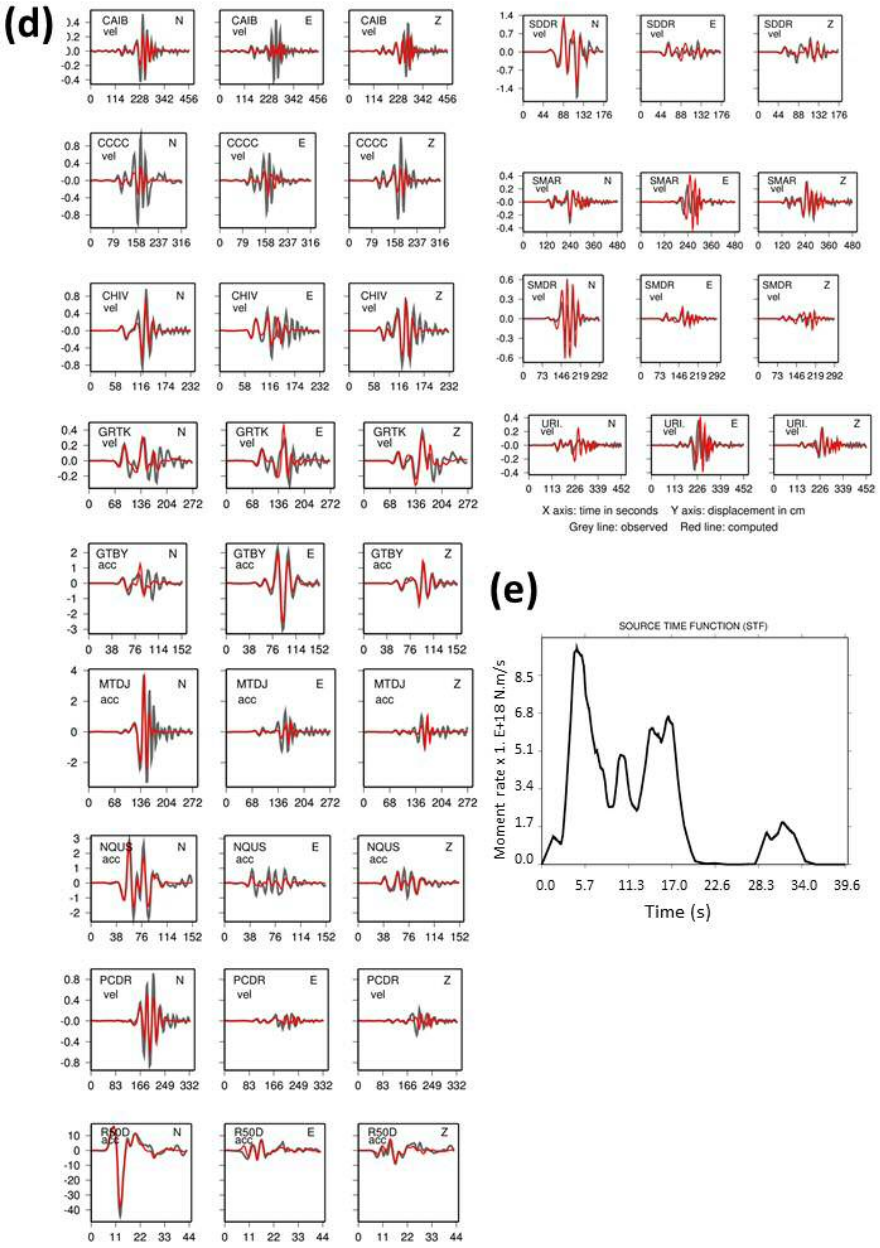

Figure S7. Result of the kinematic slip inversion for the 2021 Mw7.2 Nippes earthquake. (a) Map of stations used (green triangles), with the epicentral shown by the orange star. (b) Slip distribution. Black dots: point sources. Open triangle: hypocenter. Top: slip map. Bottom: slip vectors showing the motion of the northern bloc above the fault plane (hanging wall). (c) Slip distribution projected on the surface on a geographical map. Epicenter shown as the orange star. (d) Waveform fit, in displacement (cm) bandpass filtered (see text). Observed records are in gray and computed in red. For each station the three components are displayed (N, E, Z), and 'vel' or 'acc' means that the original record was in velocity (broadband) or in acceleration (strong motion), respectively. Station names may be truncated if they contain more than four letters. (e) Overall Source Time Function (STF) showing the seismic moment rate as a function of time.

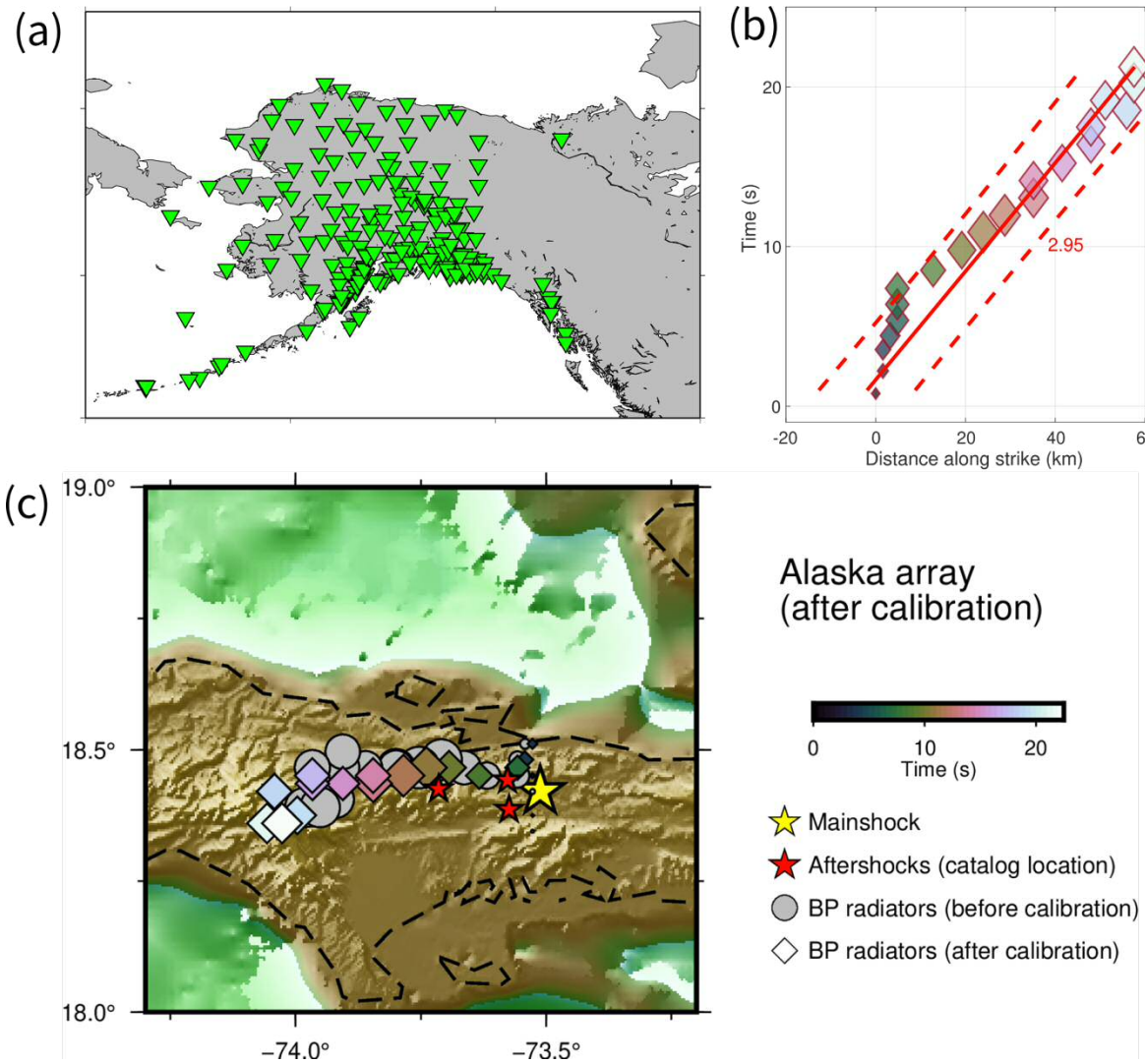

Figure S8. Teleseismic back-projection rupture imaging results. (a) Broadband stations in Alaska used in this study (green triangles). (b) The resulting high-frequency (0.25-1 Hz) radiators as a function of along-strike distance and time (considering a strike of 270°). The red line indicates a best-fitting average rupture speed of 2.95 km/s. (c) Back-projection results before and after slowness calibration. The yellow star denotes the epicenter of the Mw7.2 Haiti earthquake. Diamonds are the high-frequency radiators imaged, with size proportional to the relative energy and colored according to rupture time with respect to the mainshock origin time. The grey circles are high-frequency radiators before calibration and red stars are aftershocks used for calibration.

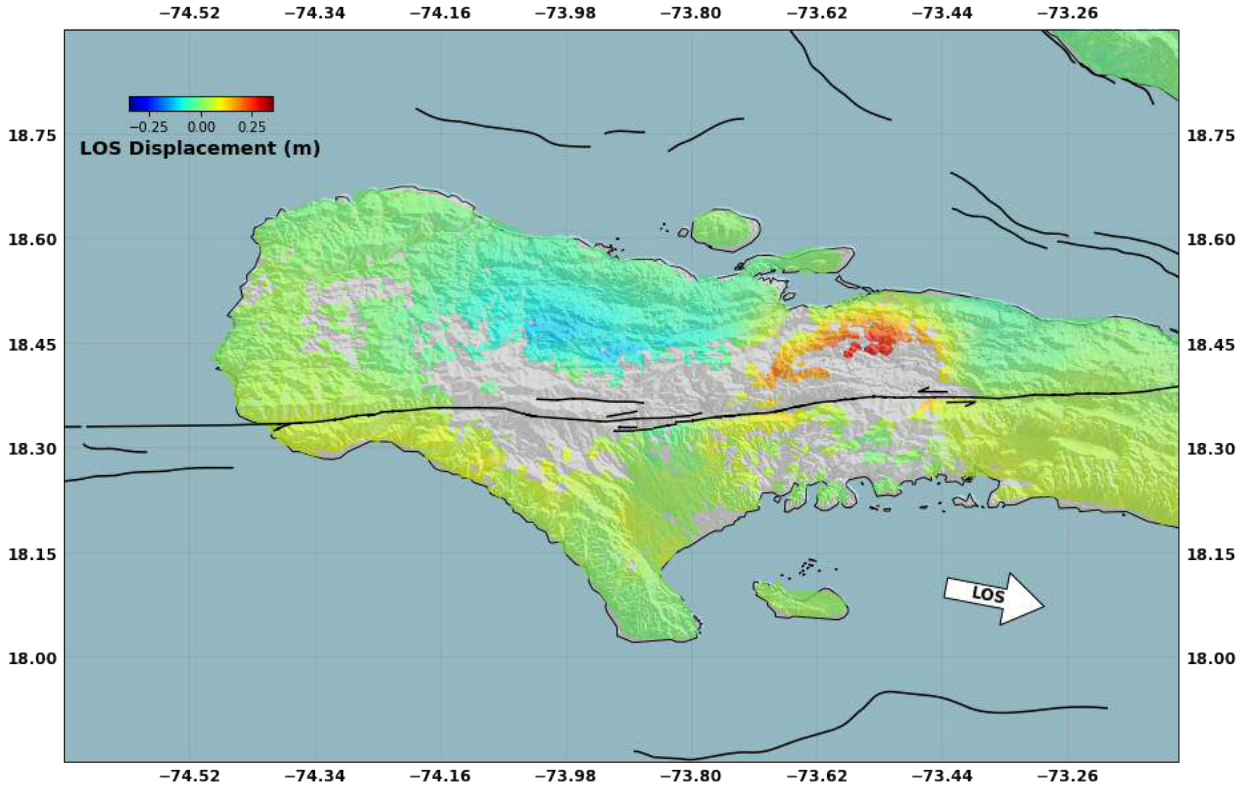

Figure S9. Displacement along the direction of the Line-Of-Sight (LOS) computed from the interferogram formed of Sentinel 1 acquisitions on August 3rd and 15th 2021. Black lines are mapped faults from *(24)*. Background shading is topography from SRTM (Farr, 2005). White arrow is the surface projection of the LOS direction pointing toward the satellite. Positive motion is toward the satellite.

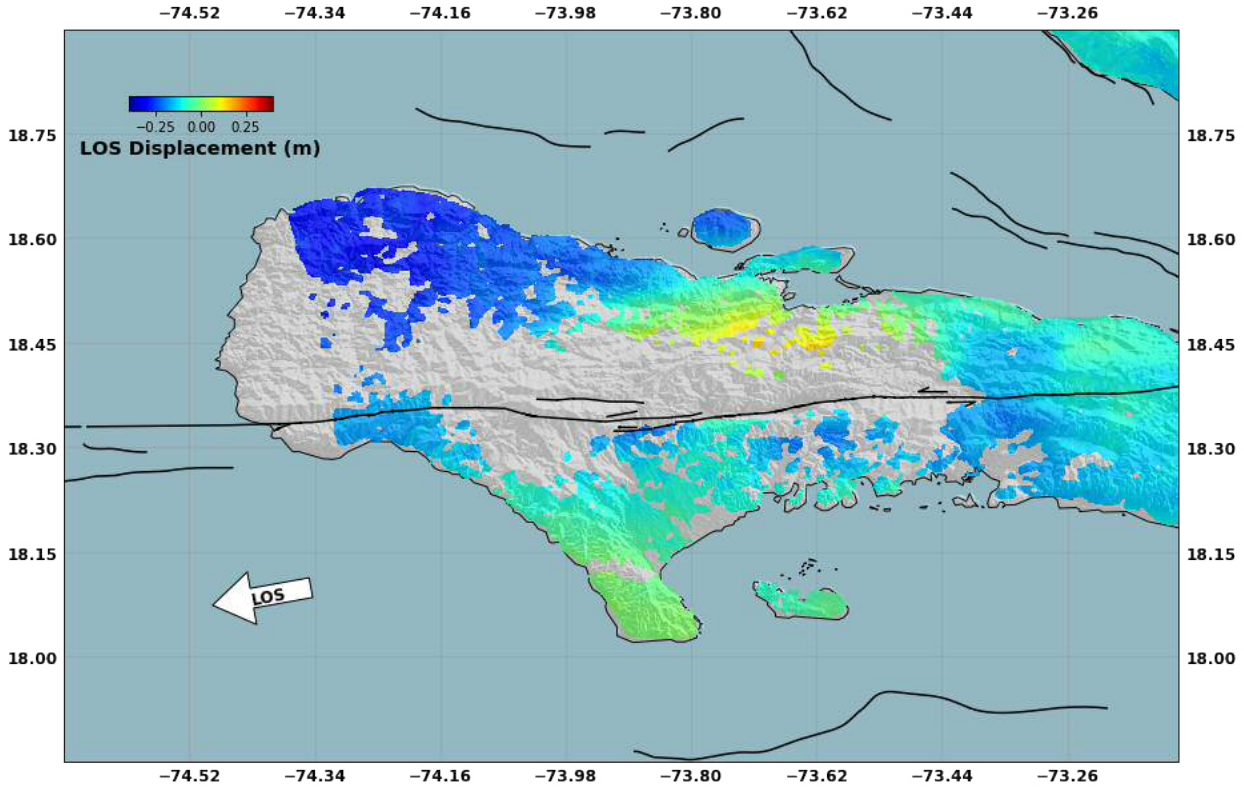

Figure S10. Displacement along the direction of the Line-Of-Sight computed from the interferogram formed of Sentinel 1 acquisitions on August 5rd and 17th 2021. Black lines are mapped faults from *(24)*. Background shading is topography from SRTM (Farr, 2005). White arrow is the surface projection of the LOS direction pointing toward the satellite. Positive motion is toward the satellite.

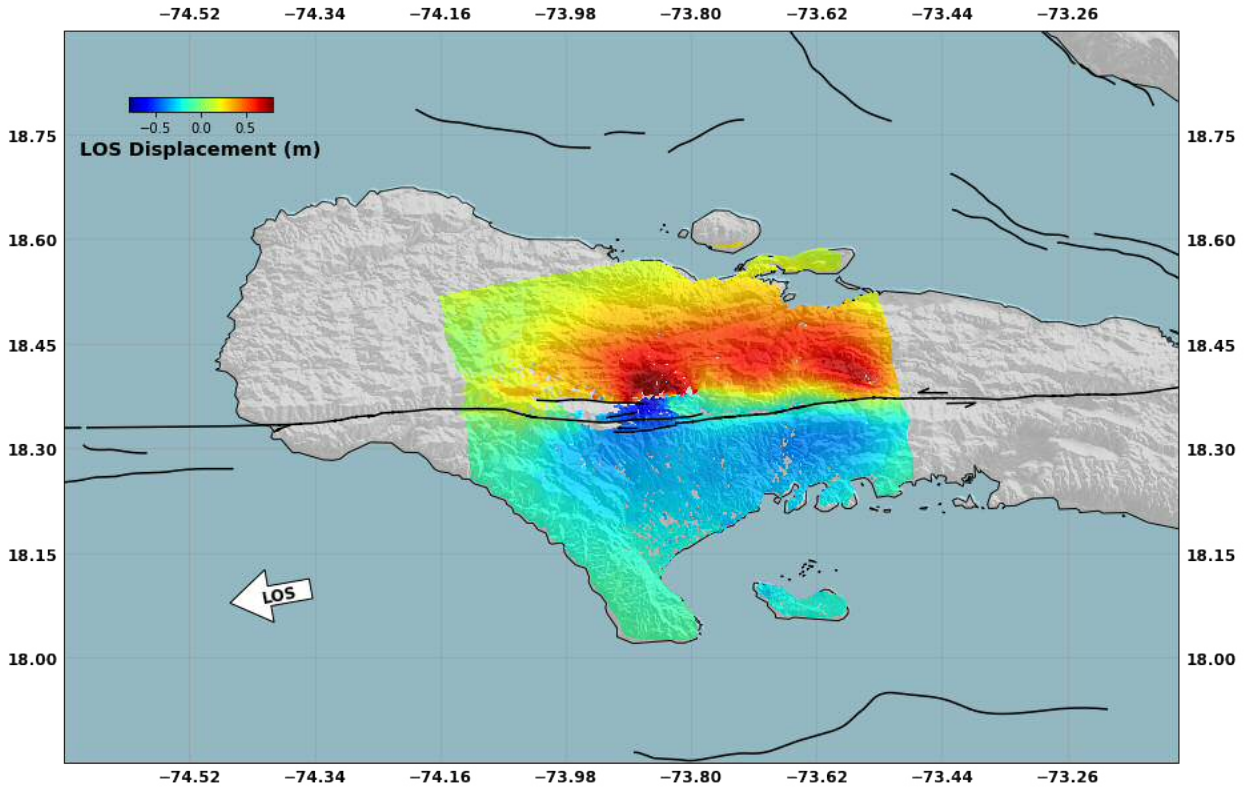

Figure S11. Displacement along the direction of the Line-Of-Sight computed from the interferogram formed of ALOS-2 acquisitions in strip map mode along an ascending track on December 23, 2020 and August 18, 2021. Black lines are mapped faults from *(24)*. Background shading is topography from SRTM ***(Error! Reference source not found.)***. White arrow is the surface projection of the LOS direction pointing toward the satellite. Positive motion is toward the satellite.

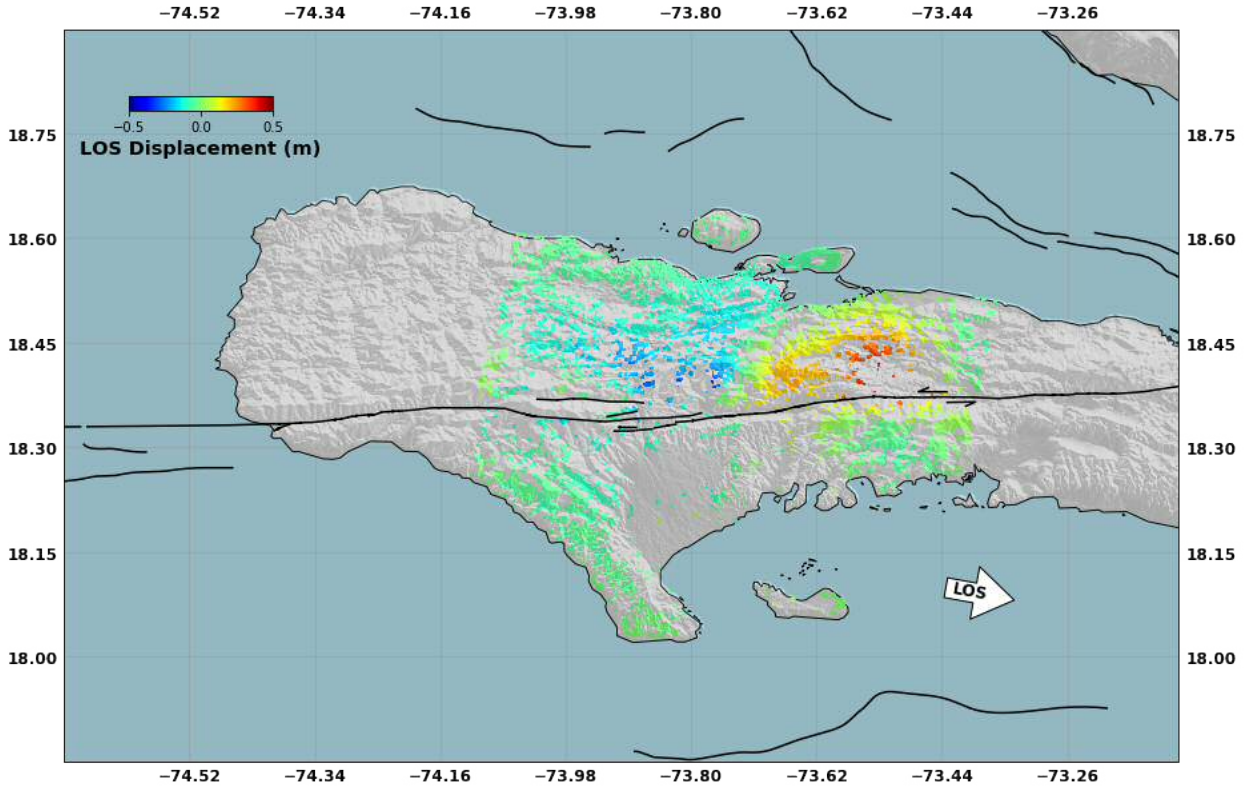

Figure S12. Displacement along the direction of the Line-Of-Sight computed from the interferogram formed of ALOS-2 acquisitions in wide-swath mode along a descending track on December 10, 2019 and August 17, 2021. Black lines are mapped faults from *(24)*. Background shading is topography from SRTM ***(Error! Reference source not found.)***. White arrow is the surface projection of the LOS direction pointing toward the satellite. Positive motion is toward the satellite. We only use swath 5 which covers the rupture.

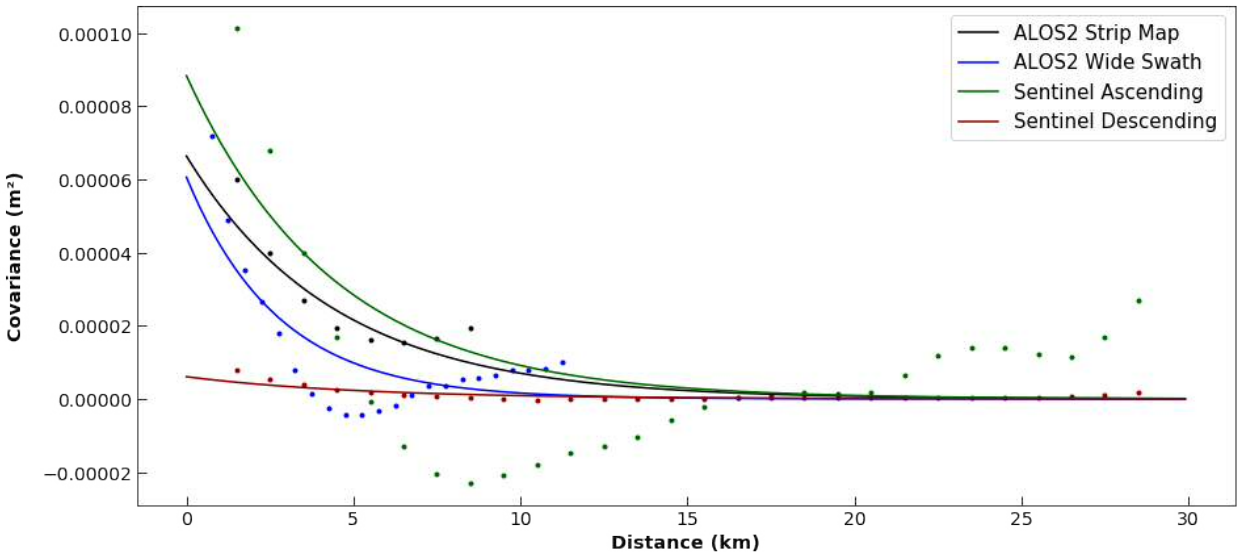

Figure S13. Empirical (dots) and modelled (lines) covariances for the four coseismic interferograms used in the slip inversions.

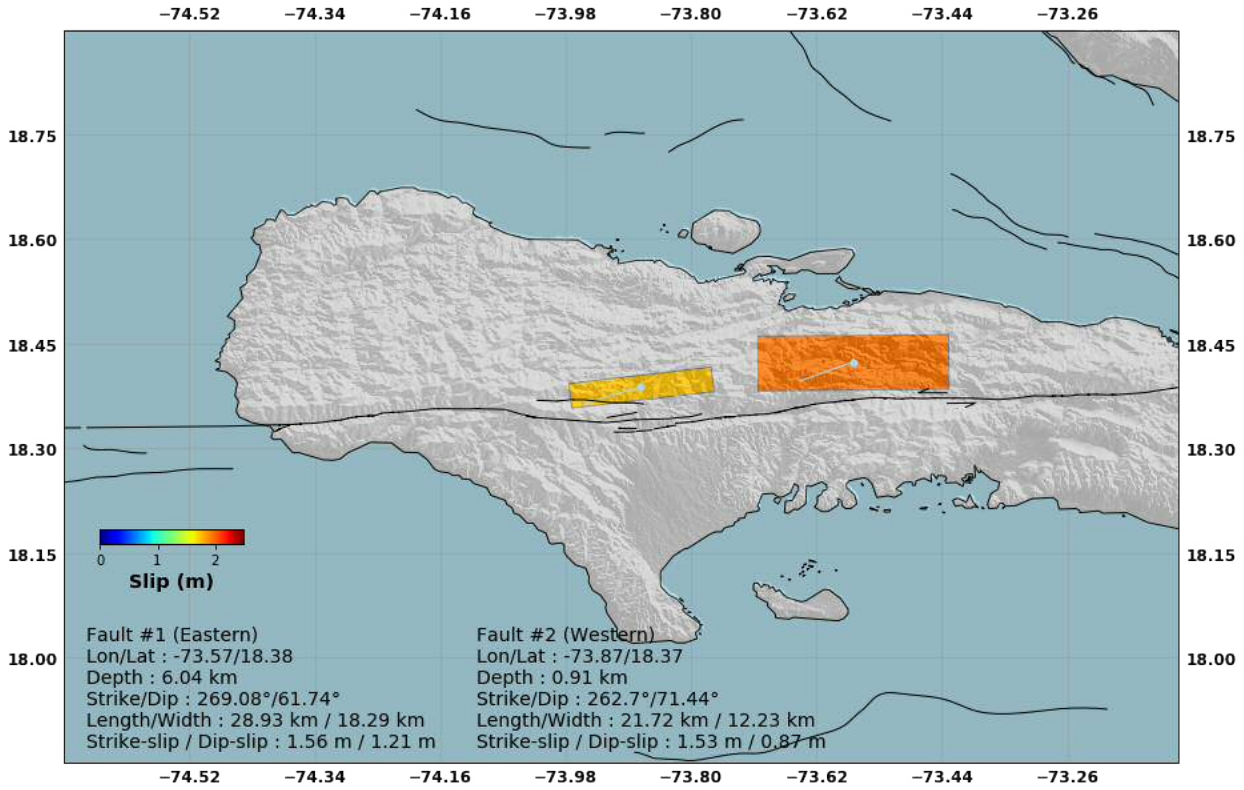

Figure S14. Best-fit solution for the two faults non-linear least squares search. Black lines are mapped faults from *(24)*. Background shading is the topography from SRTM ***(Error! Reference source not found.)***. Rectangles are the surface projection of the best fitting dislocations colored by the amount of slip requires to fit the data. Grey arrows indicate the amplitude and direction of slip on these dislocations. Details of the dislocation (center of the top side of each rectangle are indicated) are written on the figure.

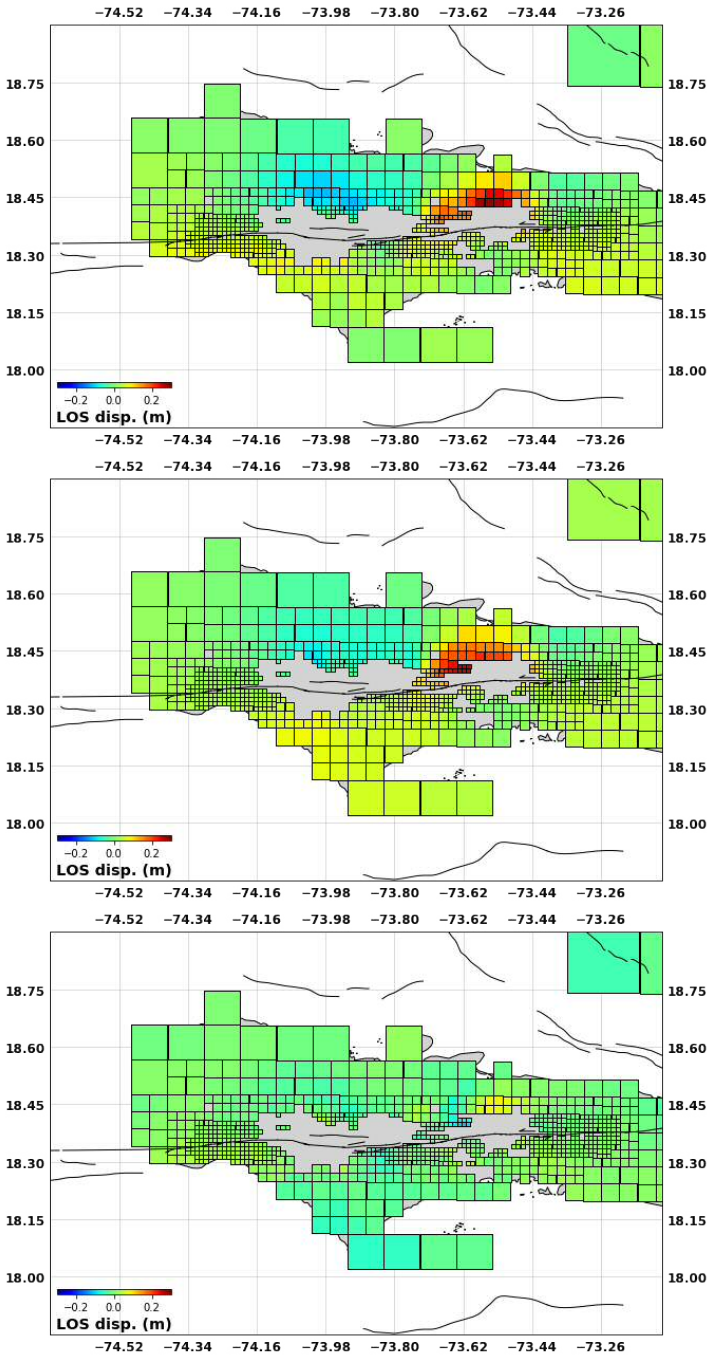

Figure S15. Model performance for the non-linear optimization searching for the most probable two faults that ruptured during the mainshock. Data (top), prediction (middle) and residuals (bottom panel) for the Sentinel coseismic interferogram on the descending track. The squares indicate the extent of the averaging windows for the quadtree down-sampling procedure.

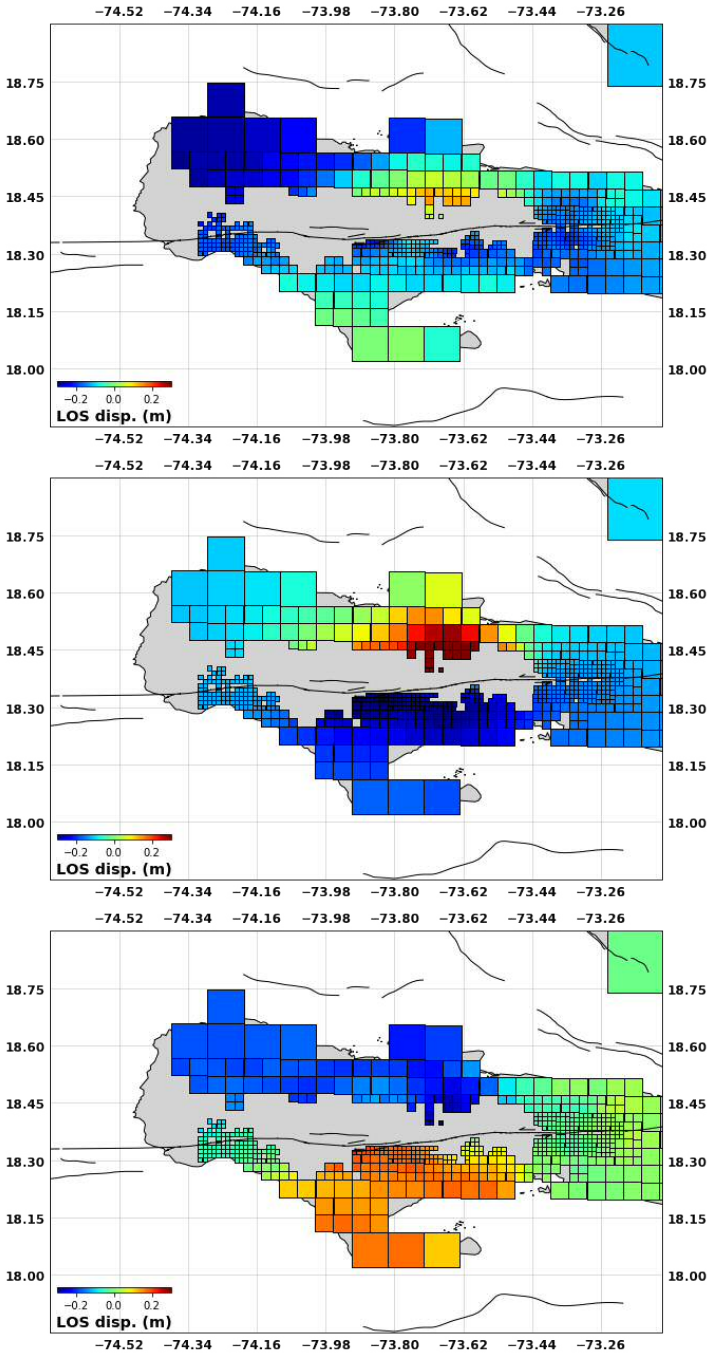

Figure S16. Model performance for the non-linear optimization searching for the most probable two faults that ruptured during the mainshock. Data (top), prediction (middle) and residuals (bottom panel) for the Sentinel coseismic interferogram on the ascending track. The squares indicate the extent of the averaging windows for the quadtree down-sampling procedure.

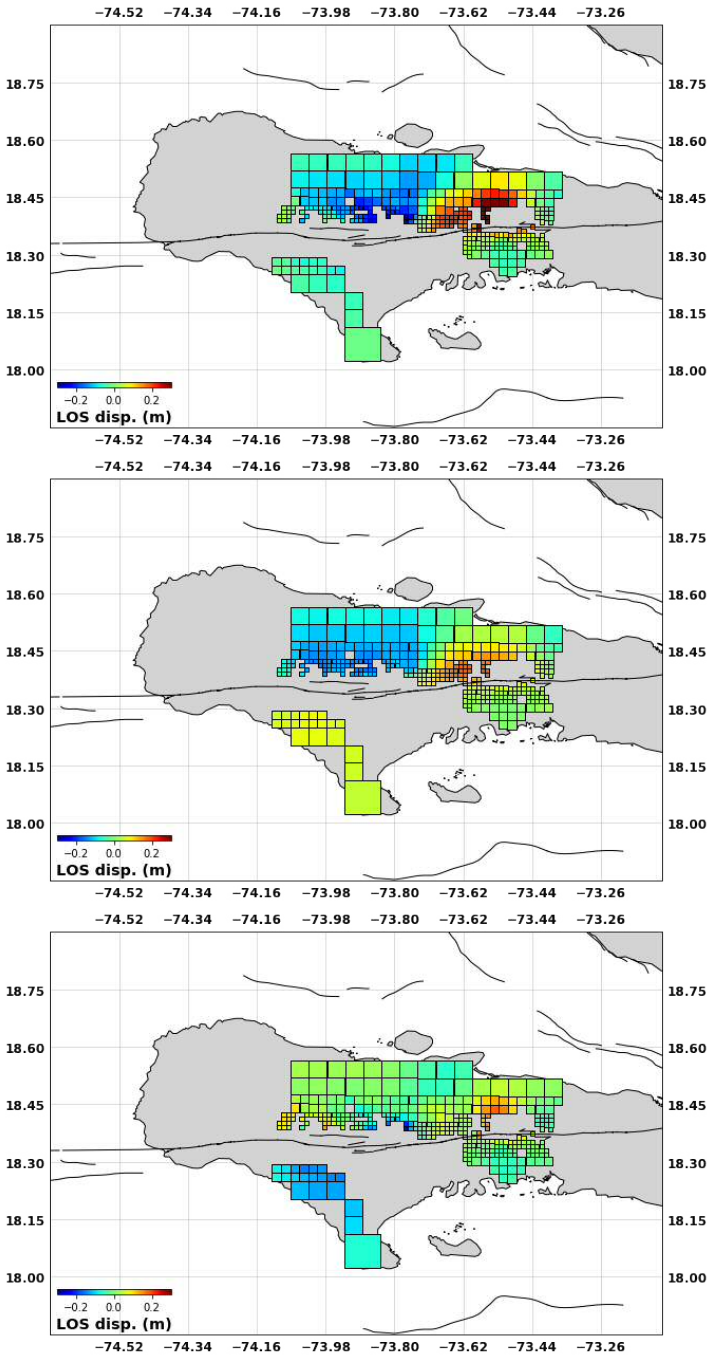

Figure S17. Model performance for the non-linear optimization searching for the most probable two faults that ruptured during the mainshock. Data (top), prediction (middle) and residuals (bottom panel) for the ALOS-2 wide swath interferogram on the descending track. The squares indicate the extent of the averaging windows for the quadtree down-sampling procedure.

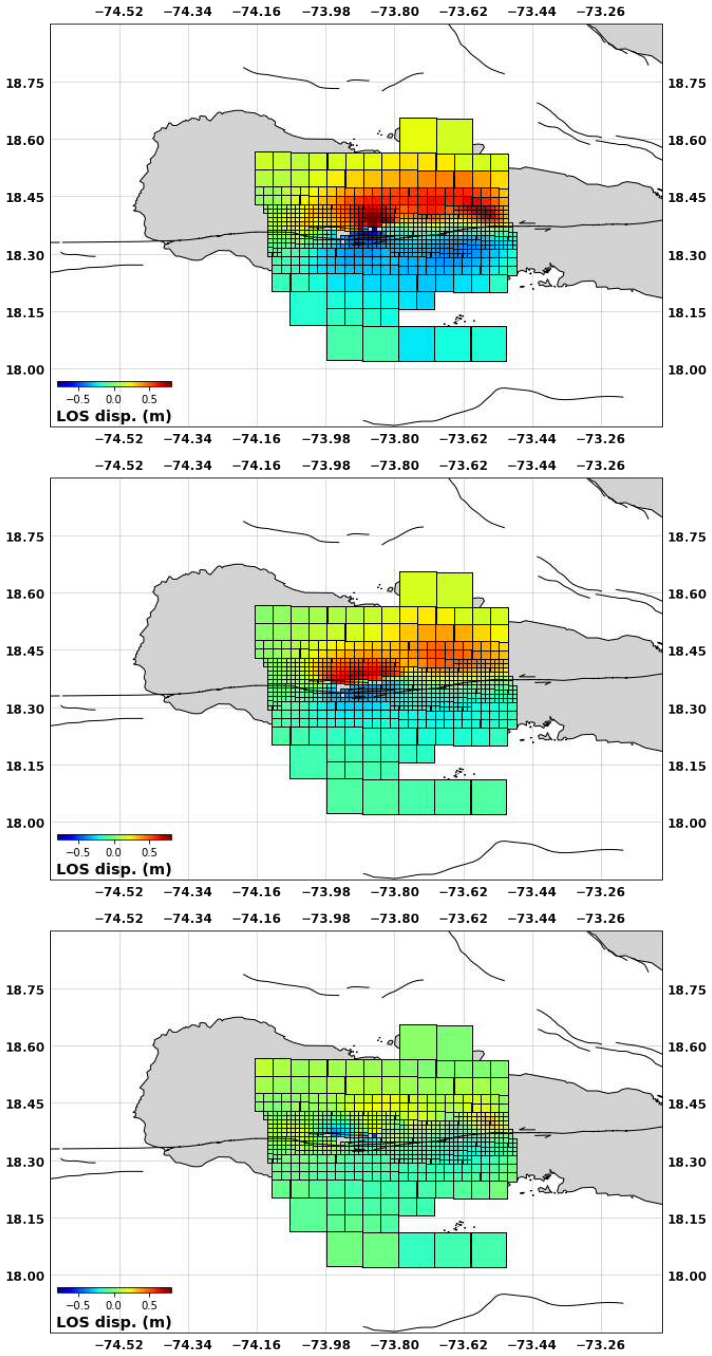

Figure S18. Model performance for the non-linear optimization searching for the most probable two faults that ruptured during the mainshock. Data (top), prediction (middle) and residuals (bottom panel) for the ALOS-2 strip map interferogram on the ascending track. The squares indicate the extent of the averaging windows for the quadtree down-sampling procedure.

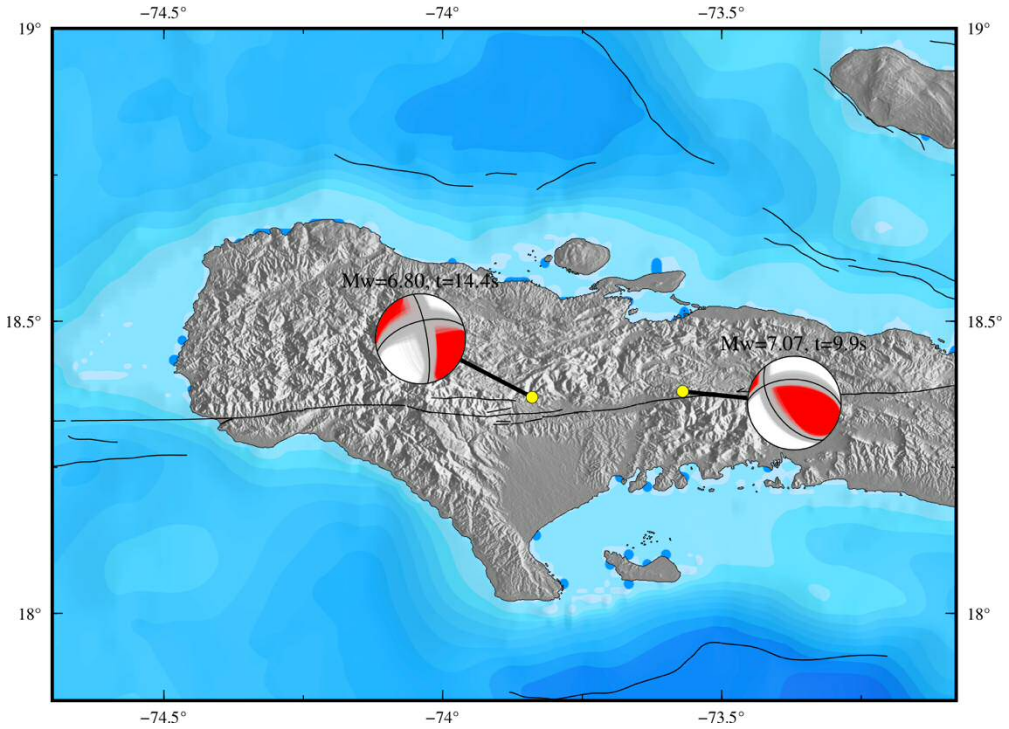

Figure S19. Two-point-source inversion. Red mechanisms represent our two point-source solution obtained from the Bayesian inversion of long-period seismic waves assuming a 3D Earth model (ref). Grey lines into the focal mechanisms indicate the posterior population of double-couple mechanisms and black lines correspond to the posterior mean model. Model performance is illustrated in Figures *S19-S21*.

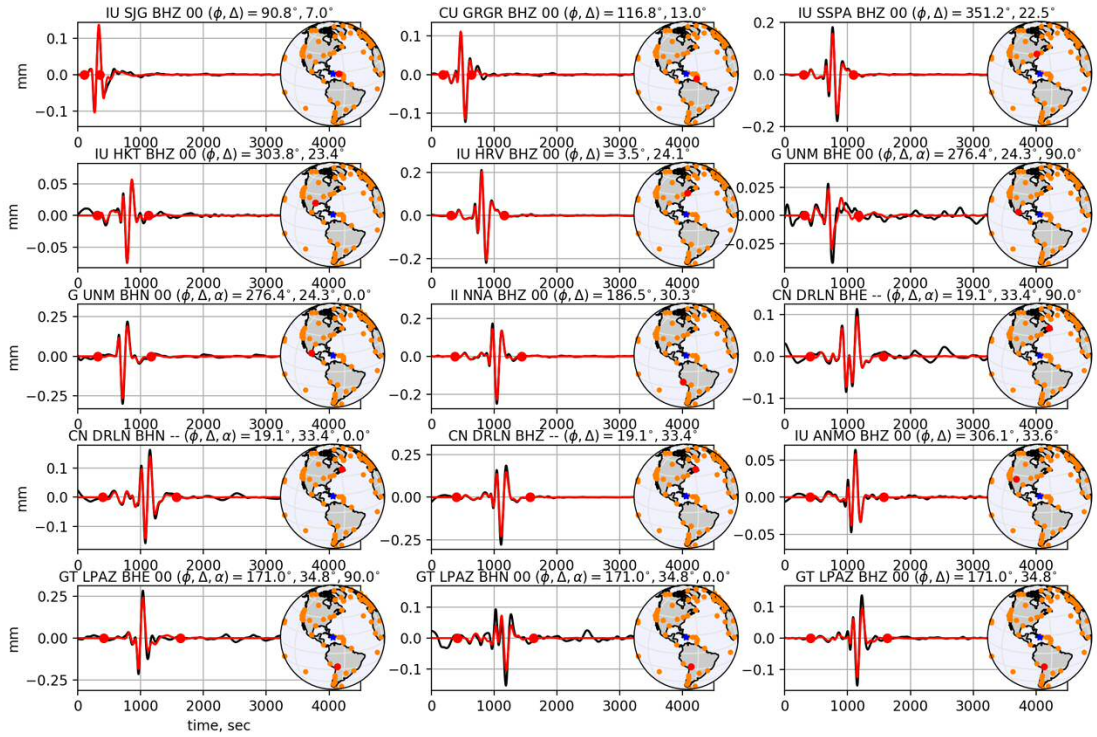

Figure S20. Example of data fitting for the two point-source model. Long period displacement waveforms (black traces) are compared to predictions for the two sub-event model (red traces). Waveforms segments used in the two-point-source inversion are bounded by red dots. Stations used for source inversion are located on the maps with orange circles. The location of the station corresponding to the plotted waveform is indicated by a red circle. Blue star is the earthquake hypocenter.

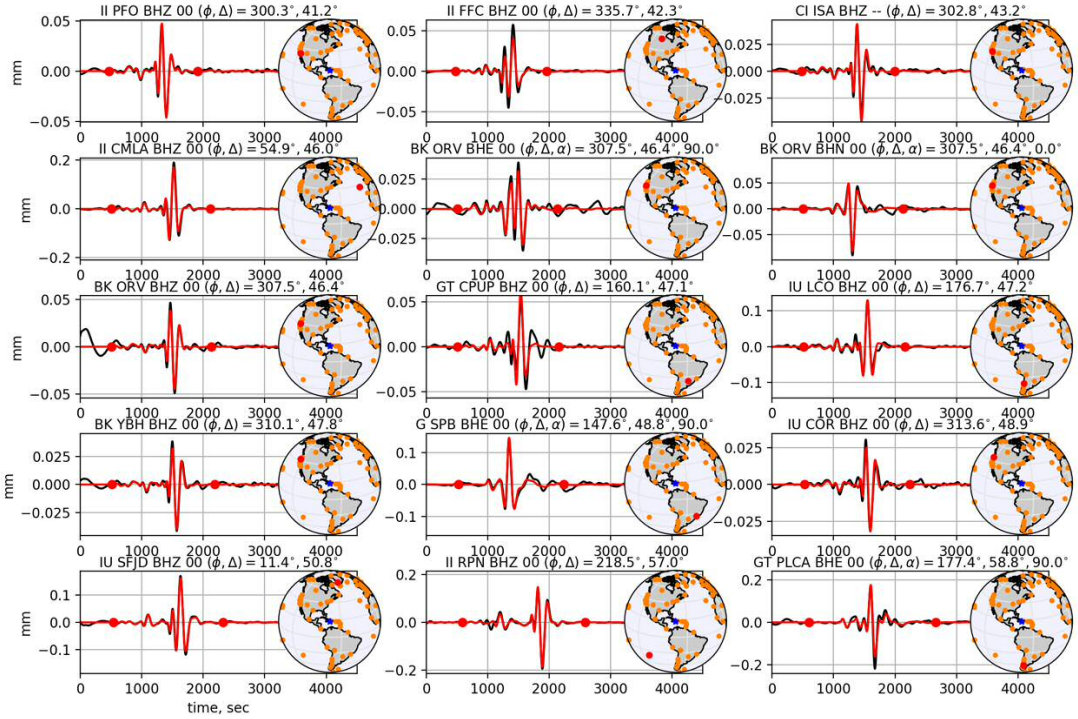

Figure S21. Same as Figure S19.

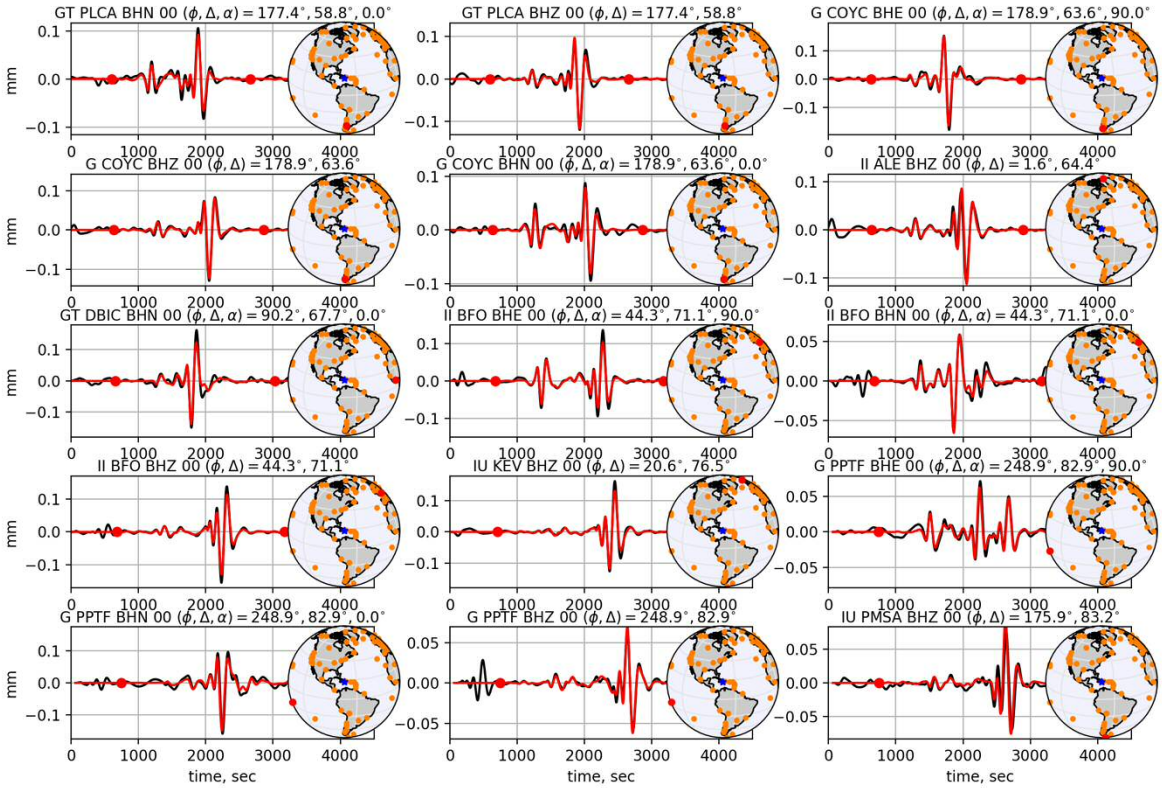

Figure S22. Same as Figure S19.

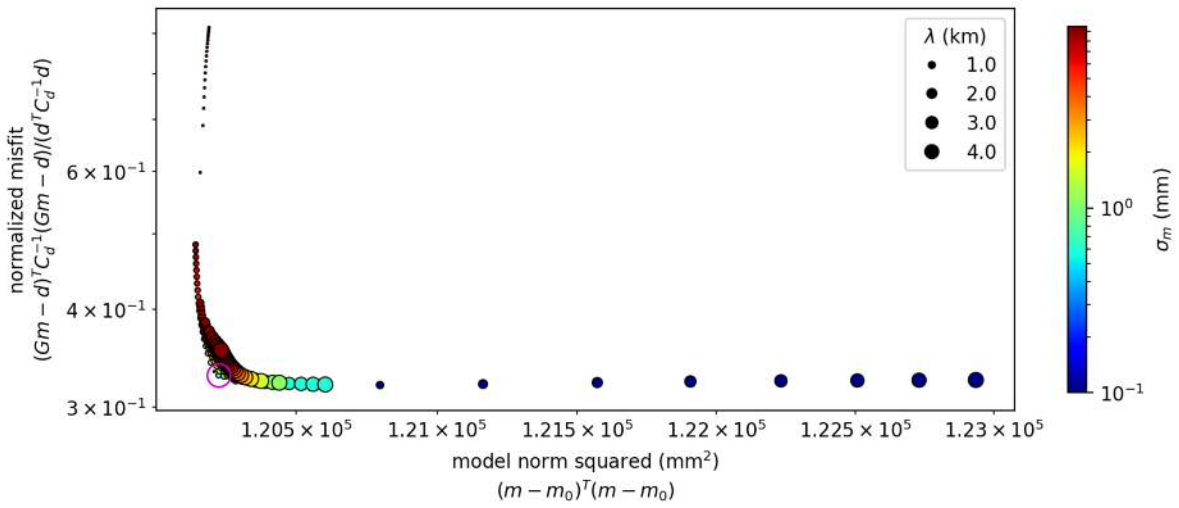

Figure S23. Normalized norm of the residuals shown as a function of the model norm for various couples of a priori model standard deviations (σ_m) and characteristic length scales (λ). The color of the dots corresponds to the standard deviation while the size refers to the length scale. We chose a [norm, misfit] couple which balances fit to the data and complexity of the model. Note that our formulation of slip on the fault introduces an inherent smoothness of the slip distribution as slip is piecewise linear and not piecewise constant over the mesh.

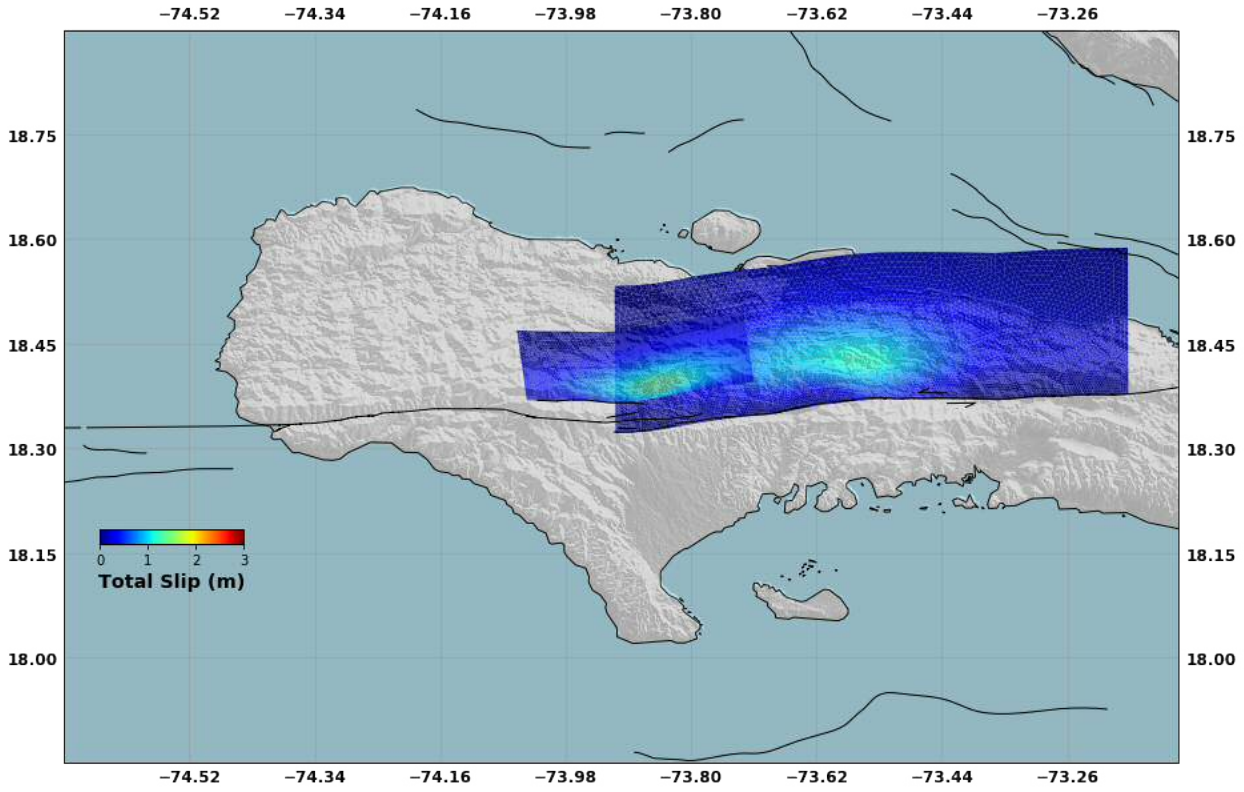

Figure S24. Example of the slip distribution obtained for an extreme case of over smoothing. All details are smeared and the fit to the data is significantly degraded. Black lines are fault traces from *(24)*. Background shading is the digital elevation model from SRTM.

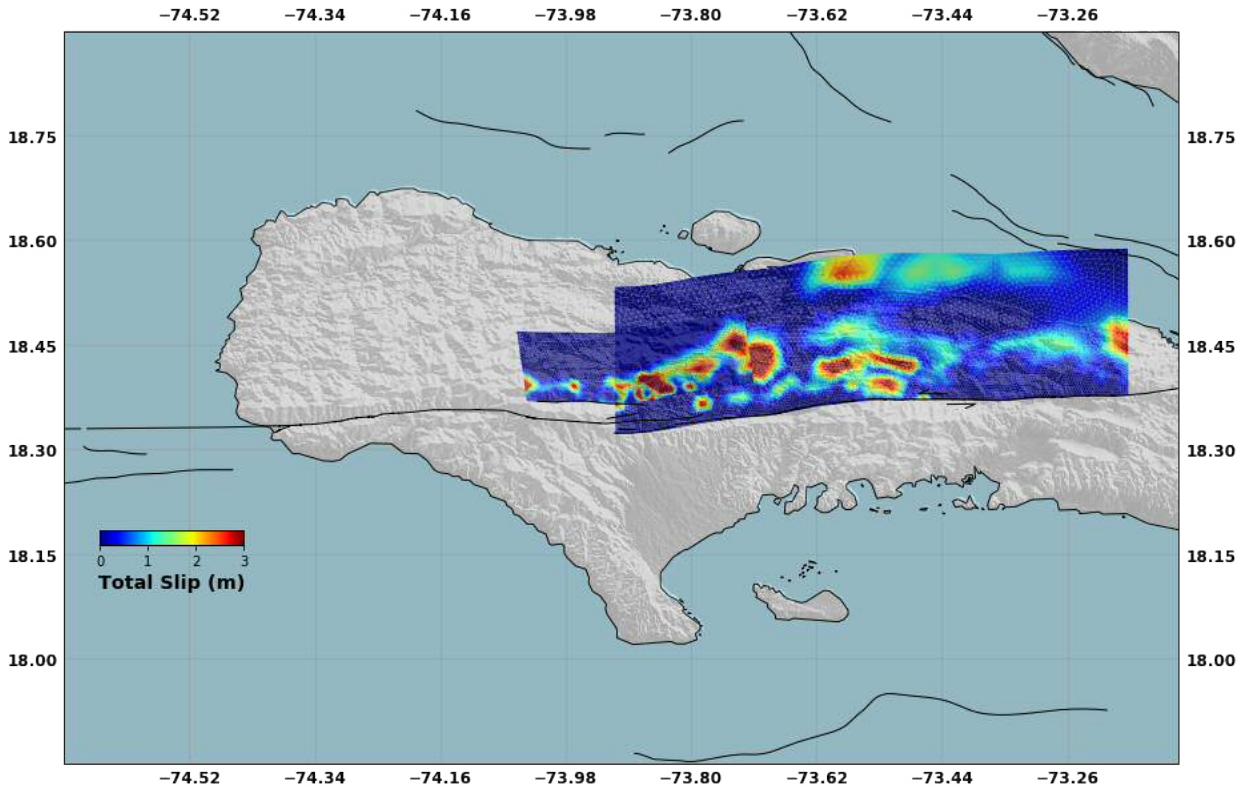

Figure S25. Example of the slip distribution obtained for an extreme case of under-smoothing. Slip pattern is almost random in order to fit all details within the data. Black lines are fault traces from *(24)*. Background shading is the digital elevation model from SRTM.

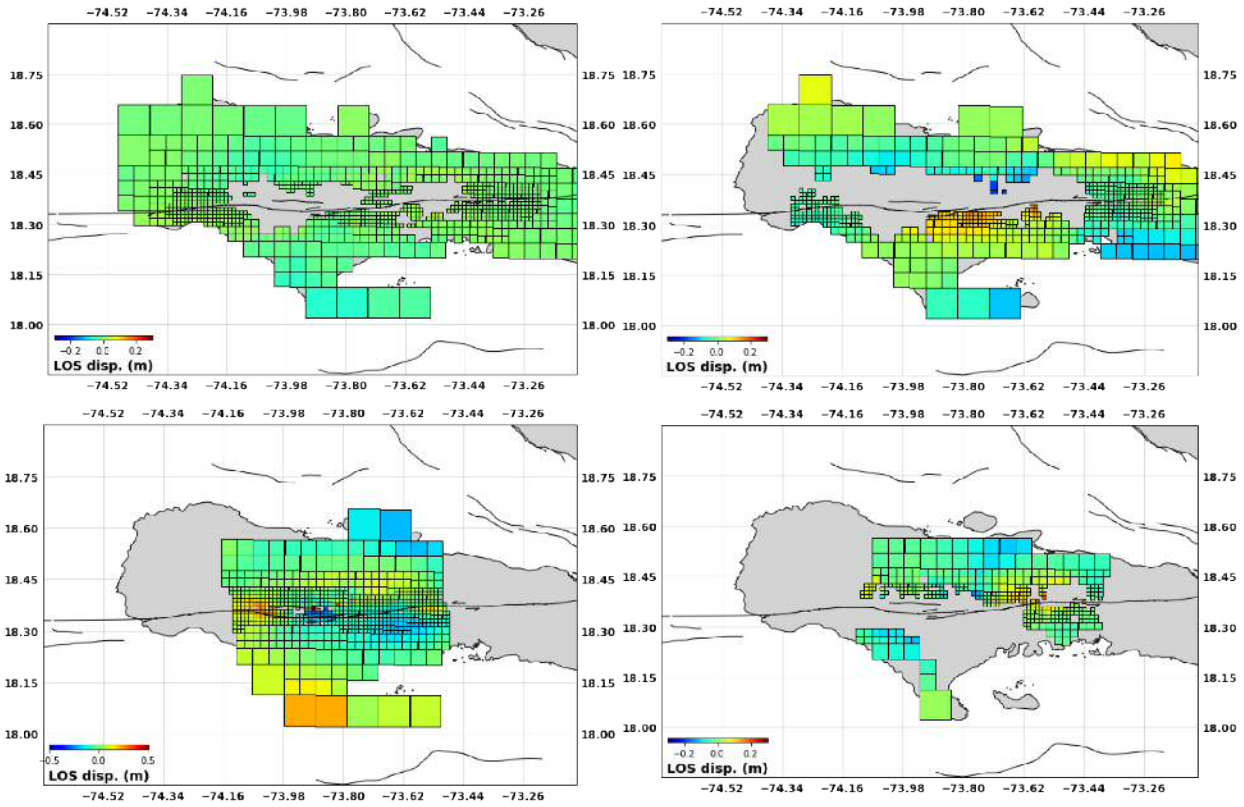

Figure S26. Data residuals for the geodetic model obtained by linear slip inversion. Note the amplitude of the residuals is much lower than that of the non-linear search.

Caption for Data S1. Catalog of high-precision earthquake relocations with the NLL-SSST-coherence procedure, as described in Supplementary Text section 4.